RSC Advances

PAPER

View Article Online
View Journal | View Issue

Cite this: *RSC Adv.*, 2025, **15**, 2958

Green synthesis of ZnO nanoparticles using *Justicia adhatoda* for photocatalytic degradation of malachite green and reduction of 4-nitrophenol

Munisha Mahajan,[a] Sanjeev Kumar,[a] Jyoti Gaur,[b] Sandeep Kaushal, *[c] Jasvir Dalal, *[d] Gurjinder Singh,[e] Mrinmoy Misra *[f] and Dharamvir Singh Ahlawat [g]

Achieving the smallest crystallite/particle size of zinc oxide nanoparticles (ZnO NPs) reported to date, measuring 5.2/12.41 nm with *Justicia adhatoda* (*J. adhatoda*) leaf extract, this study introduces a facile green synthesis. Utilizing aqueous *J. adhatoda* leaf extract as both a reducing and stabilizing agent, the method leverages the plant's rich phytochemical composition to produce highly crystalline and morphologically controlled ZnO NPs. This precise particle size control highlights the effectiveness of the synthesis process in morphological tuning. The synthesized NPs were thoroughly characterized using XRD, UV-vis spectroscopy, FTIR, FESEM, and HRTEM, which collectively revealed superior crystallinity, controlled morphology, and unique surface properties conferred by phytochemical bio-capping. The photocatalytic performance of these biogenic ZnO NPs was evaluated for the degradation of two model pollutants: malachite green (MG), a synthetic dye, and 4-nitrophenol (4-NP), a toxic organic compound. The NPs exhibited exceptional photocatalytic efficiency, achieving 99.8% MG degradation within 180 minutes and demonstrating a rapid photocatalytic reduction of 4-NP to 4-aminophenol with a reaction rate constant of 0.245 min^{-1} under UV and sunlight irradiation. Mechanistic studies attributed this high performance to reactive oxygen species (ROS) generation and electron–hole pair interactions, supported by improved charge separation and high surface area. This work not only establishes the potential of *J. adhatoda*-mediated ZnO NPs in addressing persistent organic pollutants but also sets a benchmark for size-controlled NPs synthesis. By delivering scalable and eco-friendly water remediation technologies, this study advances green nanotechnology.

Received 7th December 2024
Accepted 22nd January 2025

DOI: 10.1039/d4ra08632e

rsc.li/rsc-advances

1. Introduction

The depletion of safe water resources poses a critical environmental and public health issue, exacerbated by industrial wastewater discharges into aquatic ecosystems.[1] Among industrial activities, the textile sector has emerged as a significant contributor to global water pollution, primarily due to its extensive use of synthetic dyes. Recent estimates indicate that over 700 000 tons of textile dyes are produced annually, with azo dyes accounting for 60–70% of this volume. Commonly used azo dyes include Reactive Black 5, Acid Orange 7, and Direct Red 28, which are known for their vibrant colours and chemical stability.[2] These dyes are synthesized from aromatic hydrocarbons such as benzene, toluene, naphthalene, phenol, and aniline, components that contribute to their environmental persistence and resistance to natural degradation. Inefficiencies in dyeing processes result in the release of 15–50% of these dyes into wastewater streams, where they significantly increase the chemical oxygen demand (COD) and biological oxygen demand (BOD) of water.[3,4] Typical wastewater containing azo dyes exhibits COD values ranging from 1000 to 3000 mg L^{-1} and BOD values of 200–700 mg L^{-1}, far exceeding acceptable limits for safe discharge (50 mg L^{-1} for COD and 10 mg L^{-1} for BOD).[5] Additionally, azo dyes disrupt the physicochemical properties of water, altering its pH (typically in the range of 10–11 for dye effluents) and introducing high inorganic chemical content, which significantly impacts aquatic ecosystems.[6] Their complex molecular structures, featuring azo bonds (–N=N–) and aromatic rings, further impede degradation by conventional

[a]*Department of Physics, Chandigarh University, Gharuan, Mohali, 140413, India*
[b]*School of Basic and Applied Sciences, RIMT University, Mandi Gobindgarh, 147301, India*
[c]*Regional Institute of Education, NCERT, Ajmer, Rajasthan, 305004, India. E-mail: kaushalsandeep33@gmail.com*
[d]*Department of Physics, Rajdhani College, University of Delhi, Delhi, 110015, India. E-mail: jasvirdalal2012@gmail.com*
[e]*Department of Electrical and Electronics and Communication Engineering, DIT University, Dehradun, 248009, India*
[f]*Mechatronics Engineering Department, School of Automobile, Mechanical and Mechatronics, Manipal University, Jaipur, India. E-mail: mrinmoy.mishra@jaipur.manipal.edu*
[g]*Department of Physics, Chaudhary Devi Lal University, Sirsa, Haryana 125055, India*

water treatment methods.[7] This resistance necessitates the development of innovative and efficient solutions for their removal, particularly methods that can address their toxicity and bioaccumulation potential.[8]

Extensive advancements in nanoscience and nanotechnology have driven the development of innovative materials and advanced processes for water purification, particularly targeting the removal of toxic dyes from industrial effluents. Materials such as titanium dioxide (TiO_2), zinc oxide (ZnO), graphitic carbon nitride (g-C_3N_4), and bismuth vanadate ($BiVO_4$) have demonstrated outstanding photocatalytic properties, making them leading candidates in wastewater treatment.[9] Advanced oxidation processes (AOPs), which include ozonation, sonochemical degradation, electrochemical remediation, heterogeneous photocatalysis, and Fenton oxidation, have emerged as transformative techniques due to their ability to mineralize organic pollutants into environmentally safe byproducts like carbon dioxide and water.[10] These processes operate by generating reactive oxygen species (ROS), including hydroxyl radicals ($^{\bullet}OH$) and superoxide anions ($O_2^{-\bullet}$), which effectively break down complex dye molecules.[11]

ZnO exhibits several exceptional characteristics that distinguish it from other top-performing photocatalytic materials such as TiO_2, g-C_3N_4, $BiVO_4$, ZnS, and CeO_2.[12] With a wide direct bandgap of ~3.37 eV and a high exciton binding energy of 60 meV, ZnO ensures efficient charge carrier generation and prolonged exciton stability, outperforming TiO_2 (~4 meV), $BiVO_4$ (~20 meV), g-C_3N_4 (~30 meV), ZnS (~28 meV), and CeO_2 (~19 meV) in minimizing electron–hole recombination.[13,14] This property is critical for maintaining photocatalytic activity under UV-light irradiation. Moreover, ZnO's electron mobility, ranging from ~115–155 $cm^2\ V^{-1}\ s^{-1}$, is significantly higher than that of TiO_2 (~0.1–4 $cm^2\ V^{-1}\ s^{-1}$), $BiVO_4$ (~0.01–0.1 $cm^2\ V^{-1}\ s^{-1}$), g-C_3N_4 (~0.1–1 $cm^2\ V^{-1}\ s^{-1}$), ZnS (~5–20 $cm^2\ V^{-1}\ s^{-1}$), and CeO_2 (~4–6 $cm^2\ V^{-1}\ s^{-1}$).[15] This high electron mobility facilitates faster charge transport and supports ROS generation during photocatalytic reactions. In addition to its optical and electronic properties, ZnO demonstrates remarkable thermal and chemical stability, remaining stable up to ~1975 °C and across a wide pH range. This durability contrasts with materials prone to photo-corrosion or limited aqueous stability, such as ZnS and $BiVO_4$.[16] While CeO_2 excels in oxygen storage capacity and redox properties, its relatively narrow bandgap (~3.2 eV) can lead to undesirable secondary reactions, making ZnO a more efficient choice for photodegradation applications.[17]

In recent years, green synthesis has emerged as a cost-effective and environmentally friendly approach for developing advanced nanomaterials, particularly for applications such as photocatalytic wastewater treatment.[18] By utilizing bioactive phytochemicals present in plant extracts, this method eliminates the need for toxic chemicals and energy-intensive processes, making it a sustainable alternative to conventional techniques like sol–gel, co-precipitation, and chemical vapor deposition.[19–21] Among the numerous plant-based resources explored, *J. adhatoda* stands out as a promising candidate for NPs synthesis due to its rich phytochemical composition and medicinal properties.[22] The extract of *J. adhatoda* contains a high concentration of alkaloids (*e.g.*, vasicine and vasicinone), flavonoids (3.5 mg g^{-1} dry weight), polyphenols (42 mg g^{-1} gallic acid equivalent), terpenoids, and tannins, which act as reducing, stabilizing, and capping agents during the synthesis of ZnO NPs.[23,24] These bioactive compounds facilitate the reduction of zinc ions (Zn^{2+}) into ZnO, while the capping effect of the phytochemicals ensures particle stabilization and prevents aggregation. The hydroxyl and carboxyl groups of phenolic compounds present in the extract play a pivotal role in metal ion reduction, donating electrons to convert zinc ions into ZnO while simultaneously stabilizing the NPs through strong interactions.[25,26] The pH-adjusted synthesis process, typically conducted at pH 8, ensures optimal nucleation and growth, yielding ZnO NPs with an average size of 12.4 nm as confirmed by microscopy analysis.[27] Like studies on other plants such as *Moringa oleifera*, *Linum usitatissimum*, and *Salvadora persica*, the extract of *J. adhatoda* demonstrates the capability to produce high-quality ZnO NPs with significant photocatalytic potential. The plant's phytochemical diversity not only supports the synthesis process but also offers opportunities for tuning NPs properties to meet specific application requirements, further emphasizing its relevance in sustainable nanotechnology.[28,29]

This study is centered on the development of biogenic ZnO NPs synthesized using *J. adhatoda*, with a focus on their application in the photocatalytic degradation of malachite green (MG) and the photocatalytic reduction of 4-nitrophenol (4-NP). The novelty of this work lies in the dual evaluation of ZnO NPs for addressing distinct classes of pollutants—an industrial dye and a toxic organic compound—under UV-light irradiation. By employing a sustainable synthesis approach, this research highlights the potential of *J. adhatoda*-mediated ZnO NPs to integrate eco-friendly nanotechnology with effective wastewater treatment solutions. The ability of the synthesized ZnO NPs to achieve high degradation efficiency for both pollutants emphasizes their versatility and efficacy. Additionally, this study provides a comprehensive mechanistic understanding of the photocatalytic processes involved, shedding light on the interplay between NPs properties and pollutant degradation pathways. The work emphasizes the critical role of particle size, crystallinity, and reactive site density in enhancing photocatalytic performance. By demonstrating the successful degradation of challenging pollutants like MG and the photocatalytic reduction of 4-NP, this study sets a precedent for future research into green nanotechnology-based solutions for environmental remediation, offering a pathway toward sustainable and scalable water purification technologies.

2. Experimental details

2.1 Materials

All reagents used in this study were of analytical grade and employed without further purification. Zinc acetate dihydrate ($(CH_3COO)_2Zn_2 \cdot H_2O$: ≥99.8% purity) was used as the zinc precursor and procured from Sigma-Aldrich, Germany. Sodium hydroxide (NaOH: ≥99.7% purity) pellets were also obtained from Sigma-Aldrich and utilized to adjust the reaction conditions. Ethanol (CH_3CH_2OH: ≥98.7% purity) served as a washing agent to remove organic impurities. Fresh *J. adhatoda* leaves

were collected from a local botanical source, thoroughly washed, and processed for the preparation of the plant extract. Malachite green (MG: $C_{23}H_{25}ClN_2$, MW: 364.91 g mol^{-1}) dye, used as the test contaminant for photocatalytic experiments, was obtained from HiMedia Laboratories, India. High-purity distilled water (Emsure grade) from Fisher Scientific, Merck, was used throughout the study to ensure consistency and prevent contamination.

2.2 Preparation of *J. adhatoda* leaf extract

Fresh leaves of *J. adhatoda* were collected and gently cleaned with deionized cold water (10 °C) to remove any adhering dust or impurities. The cleaned leaves were air-dried under shade at approximately 30 °C to preserve the bioactive compounds and then pulverized into a fine powder using a mechanical grinder. This ensured uniform particle size and improved extraction efficiency. To prepare the extract, 100 g of the pulverized *J. adhatoda* leaf powder was mixed with 2 litres of deionized water in a Soxhlet extractor. The extraction process was conducted at 40 °C for 16 hours to maximize the recovery of bioactive phytochemicals, such as flavonoids, alkaloids, and terpenoids, which act as reducing and stabilizing agents. These conditions were optimized to prevent the thermal degradation of sensitive bioactive compounds (Fig. 1).

The progress of the extraction was monitored using UV-visible spectroscopy, which confirmed the stability of the phytochemical content throughout the process. The consistent absorbance spectrum of the extract indicated effective phytochemical dissolution. The pH of the extract was measured at room temperature and found to be approximately 5. The freshly prepared extract was stored in an airtight container at 4 °C to preserve its chemical stability and bioactivity. This extract was subsequently used as a reducing and capping agent for the green synthesis of ZnO NPs.

2.3 Biogenic-synthesis of ZnO NPs

ZnO NPs were synthesized using the green synthesis approach mediated by *J. adhatoda* extract (Fig. 1). This eco-friendly method utilizes the bioactive compounds in the extract to facilitate the hydrolysis of zinc ions and stabilize the NPs. To initiate the synthesis, 5 g of zinc acetate dihydrate ($(CH_3COO)_2Zn\cdot 2H_2O$) was dissolved in 15 mL of deionized water under constant stirring for 30 minutes at room temperature to ensure complete dissociation into zinc ions (Zn^{2+}). The pH of the reaction mixture was adjusted to 8 using a 0.1 M NaOH solution before the addition of the extract. This adjustment was crucial for optimizing reaction conditions, promoting zinc ion hydrolysis and ZnO NP nucleation. A pH of 8 is ideal for balancing the rate of particle nucleation and growth while avoiding excessive aggregation. Subsequently, 50 mL of *J. adhatoda* extract was added dropwise to the solution under continuous stirring. The reaction mixture was heated to 70 °C and stirred for an additional 20 minutes. A noticeable color change after 15 minutes indicated ZnO NP nucleation.

The reaction mixture was allowed to cool to room temperature and left undisturbed for 12 hours to ensure complete precipitation of the NPs. The resulting precipitate was separated by filtration using Whatman filter paper with a pore size of 1.2 μm. It was then washed three times with deionized water and

Fig. 1 Stepwise process of green synthesis of ZnO NPs mediated by *J. adhatoda* extract.

twice with ethanol to remove unreacted precursors and residual phytochemicals. After each washing step, the solution was centrifuged at 10 000 rpm for 10 minutes to recover the purified NPs. The washed ZnO NPs were dried in a hot air oven at 80 °C for 12 hours to yield a fine powder. Approximately 400 mg of ZnO NPs were obtained, corresponding to a yield of 8 mg NPs mL^{-1} of extract used. The green synthesis of ZnO NPs involves several key steps. Initially, zinc acetate dissociates in the aqueous medium, releasing zinc ions (Zn^{2+}), which act as precursors for NPs formation. Next, bioactive compounds such as flavonoids, alkaloids, and terpenoids, present in the plant extract, act as reducing agents. These compounds donate electrons to reduce zinc ions, facilitating the formation of ZnO NPs. During the process, hydroxyl ions supplied by the aqueous medium and phytochemical content form an intermediate compound, zinc hydroxide. Upon heating, zinc hydroxide undergoes dehydration, resulting in the formation of ZnO NPs. The bioactive compounds also stabilize the NPs, preventing agglomeration and ensuring uniform size distribution.

2.4 Details of characterization techniques

The structural, optical, and morphological characteristics of the synthesized ZnO NPs were investigated through comprehensive characterization. A PANalytical X'pert PRO diffractometer was used for X-ray diffraction (XRD) analysis, confirming the hexagonal wurtzite structure of the NPs by determining their crystalline phases, structural purity, and crystallite size. UV-visible spectroscopy, performed using a Shimadzu UV-2600 spectrophotometer, assessed optical properties and determined the band gap energy, revealing insights into their electronic structure. Fourier transform infrared (FTIR) spectroscopy, using a Bruker ALPHA II spectrometer, analyzed the *J. adhatoda* leaf extract and synthesized ZnO NPs to identify functional groups and interactions involved in the synthesis process. Advanced microscopy techniques provided detailed insights into particle size, surface morphology, and elemental composition. High-resolution transmission electron microscopy (HRTEM) with a Jeol JEM-2100 F microscope enabled precise measurement of particle size and morphology. Scanning electron microscopy (SEM) using a Carl Zeiss ULTRA Plus microscope offered detailed surface analysis. Energy-dispersive X-ray spectroscopy (EDX), conducted with an Oxford Instruments INCA X-act detector, confirmed the elemental composition, verifying the presence of zinc and oxygen while ensuring the absence of contaminants. These complementary techniques provided a thorough understanding of the physical and chemical properties of the ZnO NPs. Furthermore, Brunauer–Emmett–Teller (BET) surface area analysis, using a Micromeritics TriStar II analyzer, determined specific surface area, pore size, and volume-key parameters for applications such as adsorption and catalysis.

2.5 Experimental details: photocatalytic degradation of malachite green dye

The photocatalytic efficiency of the synthesized ZnO NPs was evaluated by degrading malachite green (MG) dye under UV light irradiation. A 100 mg L^{-1} aqueous solution of malachite green was prepared and used as the test contaminant. 5 mg of ZnO NPs were dispersed in 100 mL of the MG solution. The suspension was stirred in the dark for 60 minutes to establish adsorption–desorption equilibrium between the ZnO NPs and the dye molecules. The suspension was exposed to UV light from a 250 W ($\lambda = 254$ nm; germicidal UV) mercury vapor lamp positioned at a fixed distance of 15 cm. The light intensity incident on the reaction mixture was consistently measured using a radiometer, ensuring an intensity of 850 W m^{-2}, which falls within the optimal range for photocatalytic experiments.

Aliquots of 5 mL were withdrawn at regular time intervals (20, 40, 60, 80… minutes), followed by centrifugation to separate the NPs. The concentration of MG dye in the clear supernatant was analyzed using a UV-visible spectrophotometer by measuring the absorbance at 617 nm, the characteristic wavelength of MG dye. The degradation efficiency was calculated by comparing the initial concentration of MG dye at the start of the reaction (time 0) with the concentration at a specific time interval during the process.[14,30] The percentage of degradation was determined based on the reduction in dye concentration over time.

2.6 Experimental details: photocatalytic reduction of 4-nitrophenol

All reagents used in the photocatalysis experiments were of analytical grade. The ZnO NPs synthesized using *J. adhatoda* extract served as the photocatalyst. Sodium borohydride ($NaBH_4$, ≥98% purity) was purchased from Sigma-Aldrich, Germany, and used as the reducing agent. 4-Nitrophenol (4-NP, ≥99% purity) was obtained from HiMedia Laboratories, India, and prepared as an aqueous solution. High-purity deionized water (Emsure grade, Fisher Scientific) was used throughout the experiments.

The photocatalytic activity of ZnO NPs was evaluated by studying the reduction of 4-nitrophenol (4-NP) in the presence of sodium borohydride ($NaBH_4$). A reaction mixture was prepared by dissolving 4 mg of 4-NP in 100 mL of deionized water to obtain a 40 ppm solution. Subsequently, 1 mL of freshly prepared $NaBH_4$ solution (0.1 M) and 50 mg of ZnO NPs were added. The mixture was stirred gently to ensure uniform dispersion of the catalyst. The reaction mixture was placed in a quartz reactor and exposed to natural sunlight, with an intensity ranging from 800–1000 W m^{-2}. The reactor was positioned at an angle to maximize light absorption, and the temperature of the reaction system was maintained at 30 °C.

The progress of the photocatalytic reduction of 4-NP was monitored using a UV-vis spectrophotometer. Aliquots (3 mL) of the reaction mixture were withdrawn at specific intervals and immediately centrifuged at 10 000 rpm for 10 minutes to separate the NPs. The absorbance of the clear supernatant was measured in the wavelength range of 250–550 nm.

3. Results and discussion

3.1 Powder X-ray diffraction analysis

The crystalline structure and phase purity of the ZnO NPs synthesized using *J. adhatoda* extract were analyzed using X-ray diffraction (XRD). The diffraction pattern (Fig. 2(a)) exhibited sharp and well-defined peaks at 2θ values of 31.93°, 34.46°,

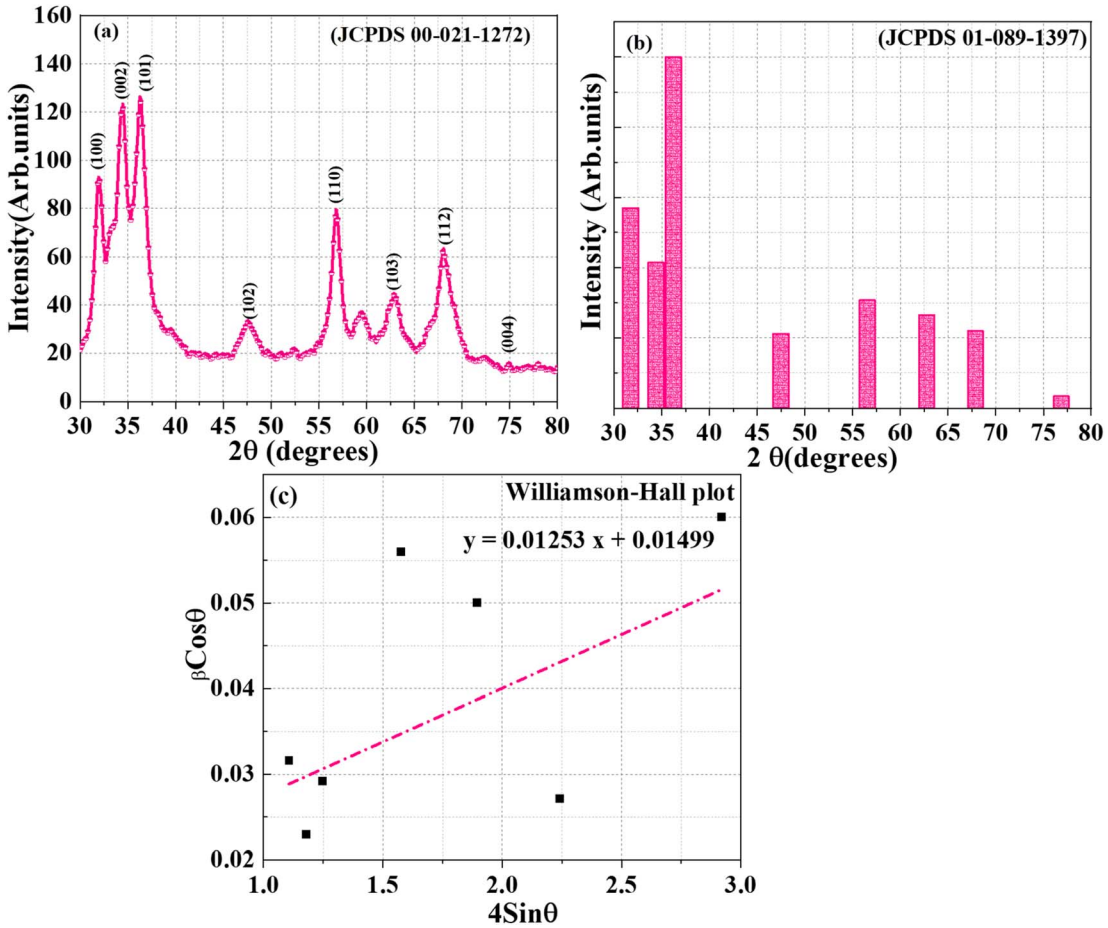

Fig. 2 X-ray diffraction spectrum of *J. adhatoda*/ZnO NPs and standard ZnO particles.

36.24°, 47.54°, 56.79°, 62.88°, 68.09°, and 77.96°, corresponding to the (100), (002), (101), (102), (110), (103), (112), and (004) lattice planes of the hexagonal wurtzite structure of ZnO, respectively (Table 1). These peaks matched the Joint Committee on Powder Diffraction Standards (JCPDS) card no. 00-021-1272 (Fig. 2(b)), confirming the formation of phase-pure

Table 1 Comparative analysis of XRD data for green synthesized ZnO NPs highlighting crystallite size, crystal structure and synthesis insights

Sr. no.	Synthesis method	Extract used	Crystallite size (nm)	Crystal structure	Key findings	References
1	Leaf extract-mediated green synthesis	*Dolichos lablab*	29	Hexagonal wurtzite	Demonstrated photocatalytic and bactericidal properties with phase-pure ZnO	31
2	Plant-mediated synthesis	*Hibiscus subdariffa*	12–18	Hexagonal wurtzite	Highlighted temperature-dependent synthesis	32
3	Aqueous extract-mediated synthesis	*Punica granatum*	10–45	Spherical, well-ordered	Reported crystallite size with antimicrobial and catalytic efficacy	33
4	Plant-mediated synthesis	Thyme leaves	35.2–243.3	Hexagonal wurtzite	Emphasized calcination effects	34
5	Plant-mediated synthesis	*Hibiscus cannabinus*	15–20	Hexagonal wurtzite	Exhibited potential in wastewater purification and antibacterial activity	35
6	Microbial-mediated synthesis	*Streptomyces baarnensis*	<12	Crystalline structure	Enhanced antibacterial efficacy using microbial-derived ZnO	36
7	Fruit extract-mediated synthesis	*Myristica fragrans*	41.23	Hexagonal wurtzite	Highlighted antifungal and photocatalytic applications	37
8	Plant-mediated synthesis	*Polyalthia longifolia*	Varied	Hexagonal wurtzite	Validated diverse synthesis conditions	38
9	Biomediated synthesis	*J. adhatoda*	5.2 (avg.)	Hexagonal wurtzite	Achieved smallest average crystallite size, strong *c*-axis orientation, and minimal lattice strain	Current study

ZnO without detectable impurities. The (100) plane at 31.93° indicated strong basal crystallinity, with an interplanar spacing (d) of 2.80082 Å and a crystallite size (D) of 7.03 nm. The intense peak at 34.46° for the (002) plane, aligned with the c-axis orientation, exhibited a spacing of 2.60050 Å and a crystallite size of 3.78 nm, indicating preferential growth along this direction—critical for piezoelectric and optical applications. The prominent (101) reflection at 36.24°, with $d = 2.47692$ Å and $D = 4.92$ nm, served as a benchmark for overall crystallinity. Higher-order reflections, such as (102), (110), and (103) at 47.54°, 56.79°, and 62.88°, revealed interplanar spacings of 1.91125 Å, 1.61979 Å, and 1.47681 Å, with crystallite sizes of 3.14 nm, 7.46 nm, and 3.64 nm, respectively, reflecting structural symmetry and lateral atomic packing. The (112) plane at 68.09°, with $d = 1.37594$ Å and $D = 4.84$ nm, provided insights into minor lattice distortions and strain effects. The high-indexed (004) plane at 77.96°, with $d = 1.22459$ Å and $D = 7.33$ nm, demonstrated long-range periodicity and structural order. The average crystallite size, determined using the Debye–Scherrer equation, was approximately 5.2 nm, indicative of nanoscale dimensions and quantum confinement effects.

The interplanar spacing (d-spacing) was calculated using Bragg's law:

$$n\lambda = 2d \sin\theta \quad (1)$$

where $n = 1$ (first-order diffraction), $\lambda = 1.5406$ Å (Cu-Kα radiation wavelength), and θ is the Bragg angle. The calculated d-values closely matched the standard ZnO lattice constants, confirming the structural integrity and crystalline quality of the NPs.

The average crystallite size (D) of the ZnO NPs was determined using the Debye–Scherrer equation:[39]

$$D = K\lambda/\beta \cos\theta \quad (2)$$

where K is the shape factor (0.9), λ is the wavelength of Cu-Kα radiation (1.5406 Å), β is the full width at half maximum (FWHM) in radians, and θ is the Bragg angle. The crystallite sizes for individual peaks are listed in Table 2. The average crystallite size was found to be 5.2 nm, suggesting that the ZnO NPs possess nanoscale dimensions. Such small particle sizes often result in quantum confinement effects, which are known to significantly alter the optical and electronic properties of the material.

To further analyze the effects of size and strain on peak broadening, Williamson–Hall (W–H) analysis was employed. The W–H method separates the size-induced and strain-induced broadening contributions based on the following equation:[40]

$$\beta \cos\theta = Dk\lambda + 4\varepsilon \sin\theta \quad (3)$$

where ε represents the strain in the lattice. By plotting $\beta \cos$ *versus* 4 $\sin\theta$, a linear fit was obtained (Fig. 2(c)), yielding a slope of 0.01253 (corresponding to strain) and an intercept of 0.01499 (size-related broadening). The crystallite size calculated from the W–H intercept was 9.25 nm, slightly larger than the value obtained from the Debye–Scherrer equation. This discrepancy underscores the importance of accounting for strain-induced broadening in nanoscale systems. The lattice strain, as determined from the slope, was found to be 0.01253, which is indicative of minor deformations due to the incorporation of phytochemicals during synthesis.

The ZnO NPs synthesized in this study using *J. adhatoda* extract exhibits an average crystallite size of 5.2 nm, which is notably smaller than those reported in similar studies (Table 1). A study provides insights into the green synthesis of ZnO NPs using Dolichos lablab leaf extract *via* a leaf extract-mediated approach. The synthesized NPs exhibited a crystallite size of approximately 29 nm and a hexagonal wurtzite structure. The study demonstrated their excellent photocatalytic activity and bactericidal properties.[31] In another research, *Hibiscus subdariffa* was used for the plant-mediated synthesis of ZnO NPs, resulting in crystallite sizes ranging from 12 to 18 nm with a hexagonal wurtzite crystal structure. This study emphasized the temperature-dependent synthesis process.[32] Another study highlights the use of an aqueous extract of *Punica granatum* to synthesize ZnO NPs and crystallite sizes between 10 and 45 nm. The research reported significant antimicrobial and catalytic efficacy of the NPs, demonstrating their potential in environmental and biomedical applications.[33] Research using thyme leaves for the green synthesis of ZnO NPs emphasized the role of calcination temperature in determining their structural properties. The crystallite sizes varied from 35.2 to 243.3 nm, with a hexagonal wurtzite crystal structure.[34] A study using *Hibiscus*

Table 2 Crystallographic parameters of *J. adhatoda*/ZnO NPs

Sr. no	2θ (degree)	FWHM (β) (degree)	Lattice planes (hkl)	Inter-planner spacing (d) (Å)	Crystallite size (D) (nm)
1	31.93	1.22809	(100)	2.80082	7.03
2	34.46	2.29841	(002)	2.60050	3.78
3	36.24	1.77468	(101)	2.47692	4.92
4	47.54	2.88408	(102)	1.91125	3.14
5	56.79	1.26491	(110)	1.61979	7.46
6	62.88	2.67535	(103)	1.47681	3.64
7	68.09	2.06760	(112)	1.37594	4.84
8	77.96	1.45530	(004)	1.22459	7.33
				D (average) = 5.2 nm	

Table 3 Lattice parameters and unit cell volume of *J. adhatoda*/ZnO NPs

Lattice constants	Standard values (Å)	Calculated values (Å)	*c*/*a* ratio	Standard volume (Å)^3	Calculated volume (Å)^3
$a = b$	3.2498	4.8	1.0	47.62	192.3
c	5.2066	5.2			

cannabinus for plant-mediated synthesis produced ZnO NPs with a crystallite size ranging from 15 to 20 nm and a hexagonal wurtzite structure.[35] In microbial-mediated synthesis, *Streptomyces baarnensis* was used to produce ZnO NPs with crystallite sizes below 12 nm.[36] Another study utilized *Myristica fragrans* fruit extract for the synthesis of ZnO NPs, resulting in a crystallite size of 41.23 nm with a hexagonal wurtzite structure. This research demonstrated the NPs' antifungal and photocatalytic properties.[37] In another research, *Polyalthia longifolia* was employed for plant-mediated synthesis, resulting in ZnO NPs with varied crystallite sizes and a hexagonal wurtzite structure.[38] Although their study achieved moderate crystallinity and smaller sizes than most chemical methods, the particles were still larger than those produced in the current work.

The reduced crystallite size of the ZnO NPs can be attributed to the bio-template role of the *J. adhatoda* extract, which contains alkaloids, flavonoids, and other phytochemicals. These biomolecules act as capping and stabilizing agents, preventing particle agglomeration and promoting the formation of well-crystallized, nanoscale particles. Furthermore, the use of *J. adhatoda* extract enhances the ecological sustainability of the synthesis process by eliminating the need for toxic chemical stabilizers.

Notable structural differences are observed between the estimated and standard lattice values, likely caused by synthesis-induced effects. While the *c*-axis value (5.2 Å) closely matches the standard (5.2066 Å), indicating intact symmetry along this direction, the computed $a = b$ value (4.8 Å) is significantly larger than the standard (3.2498 Å), suggesting probable lattice expansion due to strain, defects, or doping (Table 3). Minimal hexagonal distortion is evidenced by the optimal *c*/*a* ratio of 1.0, which reinforces the structural stability of the wurtzite phase. The unit cell volume, calculated at 192.3 Å^3 compared to the standard 47.62 Å^3, indicates significant volumetric expansion, likely due to doping or lattice strain. These variations underscore the impact of synthesis parameters on structural characteristics, which can influence material performance in applications such as optoelectronics and photocatalysis.

Thus, the XRD and W–H analyses confirm the successful synthesis of hexagonal wurtzite ZnO NPs with nanoscale dimensions, strain effects, and high crystallinity. The synergistic effect of phytochemical-mediated synthesis ensures the controlled growth of ZnO NPs with superior structural and morphological properties, making them suitable for advanced applications in catalysis, optoelectronics, and biomedicine.

3.2 UV-visible absorption analysis

The optical properties of ZnO NPs synthesized using *J. adhatoda* extract were investigated *via* UV-visible spectroscopy. The absorption spectrum, as shown in Fig. 3(a), exhibits a distinct absorption peak at approximately 353 nm, indicative of the band-edge absorption of ZnO NPs—a characteristic feature of their electronic structure. This absorption peak is blue-shifted relative to bulk ZnO's band edge (~375 nm), a shift attributed to the quantum confinement effect. This phenomenon occurs when the particle size approaches or is smaller than the Bohr exciton radius of ZnO (~2.9 nm). The spatial confinement of charge carriers (electrons and holes) within the NPs increases energy levels, widening the bandgap and shifting absorption to shorter wavelengths.[41] The sharpness and intensity of the peak suggest a high degree of uniformity and crystallinity in the NPs, as well as effective stabilization by phytochemicals present in the *J. adhatoda* extract. These phytochemicals, including flavonoids, alkaloids, and terpenoids, act as capping agents, minimizing surface defects and enhancing optical properties.

The UV absorption observed in this study aligns with findings from prior green synthesis research. The comparative analysis presented in Table 4 highlights the superior optical properties of ZnO NPs synthesized using *J. adhatoda* extract in this study. With an absorption peak at 353 nm and a bandgap energy of 3.09 eV, the synthesized NPs achieve an optimal balance between bandgap tuning and quantum confinement effects, surpassing several prior reports. For instance, while Pandiyan (2019) reported a bandgap of 3.11 eV for *J. adhatoda*-derived ZnO NPs, the present study achieves a slightly reduced bandgap, indicating enhanced optical efficiency. Similarly, compared to NPs derived from *Moringa oleifera* (3.08 eV) and *Aloe vera* (3.10 eV), the current synthesis process yields ZnO NPs with tailored bandgap energies, making them more suitable for applications requiring precise UV absorption and efficient charge carrier generation.

In contrast, plant-mediated syntheses using *Eucalyptus globulus* (2.67 eV) and *Allium cepa* (2.66–2.79 eV) exhibit significantly lower bandgap energies, limiting their suitability for high-energy applications. Meanwhile, *Mimosa pudica*-derived NPs, with a bandgap of 3.50 eV, display excessive quantum confinement, reducing their absorption range. These results underscore the superiority of the *J. adhatoda*-mediated synthesis presented here, achieving a desirable combination of a blue-shifted absorption peak and a moderately reduced bandgap. This makes the synthesized ZnO NPs particularly suitable for advanced optoelectronic, photocatalytic, and UV-blocking applications. The findings emphasize the effectiveness of the synthesis method employed in this study in producing highly crystalline, uniform ZnO NPs with enhanced optical properties.

The analysis of Fig. 3(b) was conducted to gain deeper insights into the optical properties of the ZnO NPs. Tauc plot,

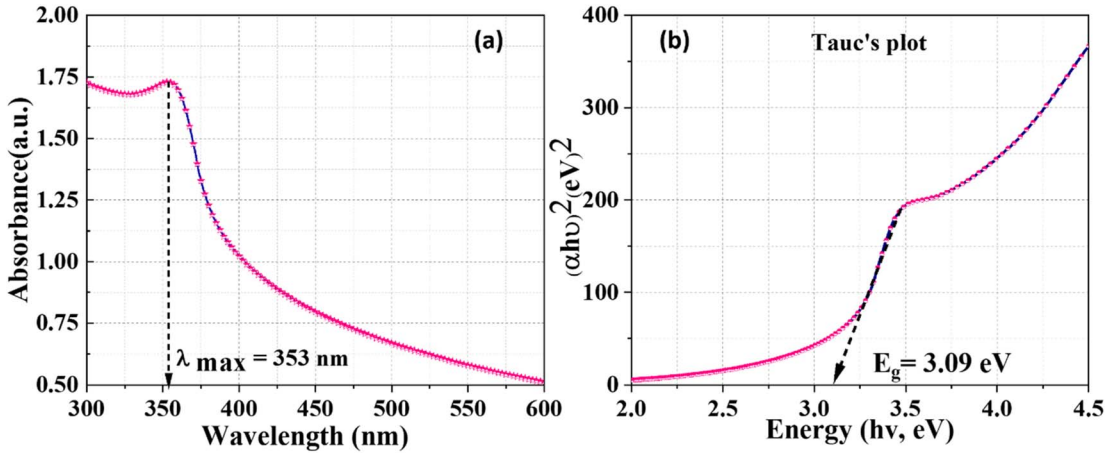

Fig. 3 Optical study *J. adhatoda*/ZnO NPs: (a) UV-visible absorption spectrum and (b) and Tauc plot.

Table 4 Comparative analysis of ZnO NPs synthesized using various plant extracts, highlighting absorption peaks, and bandgap energies

Order	Plant extract used	Absorption peak (nm)	Bandgap energy (eV)	Reference
1	*Justicia adhatoda*	355	3.11	42
2	*Moringa oleifera*	358	3.08	43
3	*Aloe vera*	200–450	3.10	44
4	*Azadirachta indica*	200–450	3.12	
5	*Amaranthus dubius*	200–450	3.07	
6	*Calendula officinalis*	355 and 370	2.986	45
7	Algerian date syrup	NA	3.19	46
8	*Eucalyptus globulus*	464	2.67	47
9	*Allium cepa* (onion bulb)	445	2.66–2.79	48
10	*Mimosa pudica*	300	3.50	49
11	*J. adhatoda*	353	3.09	Present study

which correlates optical absorbance data with photon energy ($h\nu$), was used to determine the bandgap energy (E_g). By plotting $(\alpha h\nu)^2$ as a function of $h\nu$ and extrapolating the linear portion of the curve to the x-axis, the bandgap energy of the synthesized ZnO NPs was calculated to be 3.09 eV, smaller than the bulk ZnO bandgap (3.37 eV). This reduction can be attributed to the influence of surface defects, phytochemical interactions, and mild synthesis conditions. Surface-bound phytochemicals may introduce localized energy states within the bandgap, effectively narrowing the measured bandgap. Additionally, defect states, such as oxygen vacancies and particle aggregation, could further contribute to this deviation from quantum confinement effects. This behaviour aligns with prior studies of green-synthesized ZnO, which highlight the complexity of interpreting optical properties in phytochemically mediated syntheses.

The decreased bandgap energy is advantageous for applications requiring higher UV absorption, such as photocatalytic degradation of organic pollutants, optoelectronic devices, and UV-blocking materials.[50] This bandgap enhancement ensures better utilization of UV light for generating charge carriers, a critical feature for improving the efficiency of photocatalysts.

Therefore, the results from Fig. 3(a) and (b) validate that the green synthesis of ZnO NPs using *J. adhatoda* extract produces NPs with tailored optical properties, including a blue-shifted absorption edge and an enhanced bandgap energy. These findings highlight the influence of the phytochemical-mediated synthesis process in achieving nanoscale effects, rendering the material suitable for advanced applications in environmental remediation, optoelectronics, and antimicrobial treatments.

3.3 FTIR analysis

The FTIR spectra of *J. adhatoda* extract and *J. adhatoda*-mediated ZnO NPs provide valuable insights into the functional groups involved in the synthesis and stabilization of the NPs. The FTIR spectrum of *J. adhatoda* extract (Fig. 4(a)) exhibits characteristic peaks at 3739 cm^{-1}, 3426 cm^{-1}, and 2892 cm^{-1} corresponding to O–H stretching of alcohols, N–H stretching of amines, and C–H stretching vibrations of alkanes, respectively.[51] Peaks at 2371 cm^{-1} and 1686 cm^{-1} are assigned to C≡N stretching of nitriles and C=O stretching vibrations of ketones, while the bands at 1516 cm^{-1} and 654 cm^{-1} indicate N–H bending of amides and C–C stretching, respectively.[52] These peaks confirm the presence of bioactive phytochemical constituents such as flavonoids, alkaloids, and terpenoids, which play a crucial role in reducing and capping the ZnO NPs.[53]

The FTIR spectrum of the *J. adhatoda*/ZnO NPs (Fig. 4(b)) reveals significant shifts and the emergence of new peaks,

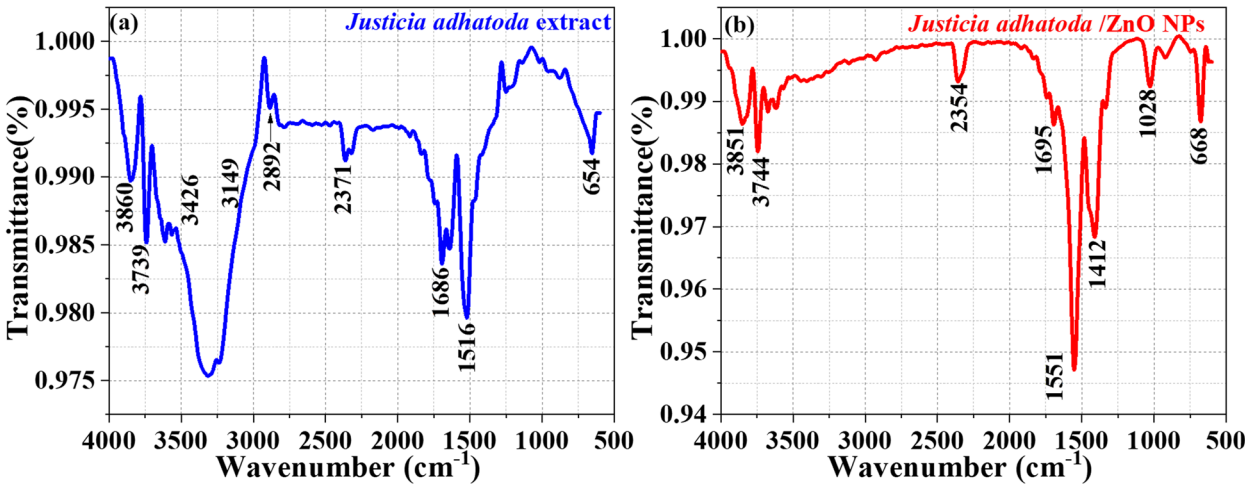

Fig. 4 FTIR spectrum: (a) *J. adhatoda* extract and (b) *J. adhatoda*/ZnO NPs.

indicating the successful formation of NPs and the interaction between phytochemicals and the ZnO surface. The stretching vibrations of the –OH and –NH groups of polyols and amides are responsible for a high absorption at 3451 cm^{-1}.[54] The peak at 2354 cm^{-1} represents C≡N stretching, while the bands at 1695 cm^{-1} and 1551 cm^{-1} are attributed to C=O stretching and N–H bending, respectively. Notably, the sharp peak at 1028 cm^{-1} corresponds to the Zn–O stretching vibration, confirming the formation of ZnO NPs. The peak at 668 cm^{-1} further corroborates the Zn–O bond, indicating the successful synthesis of ZnO NPs.[55]

The shifts in peak positions and changes in intensity between the spectra of the extract and the ZnO NPs demonstrate the active involvement of phytochemicals in reducing zinc ions to ZnO and stabilizing the NPs.[56] These findings align with reports in the literature, where bioactive compounds such as alkaloids and flavonoids have been shown to act as natural reducing and capping agents, ensuring the stability and uniformity of NPs. The use of *J. adhatoda* in green synthesis provides a biocompatible and eco-friendly approach, with potential applications in photocatalysis, antimicrobial activity, and environmental remediation.[57] This FTIR analysis highlights the role of phytochemicals in mediating NPs synthesis and highlights the functional integrity of the synthesized ZnO NPs.

3.4 FESEM analysis

The surface morphology, size distribution, and elemental composition of *J. adhatoda*-mediated ZnO NPs were analyzed using field emission scanning electron microscopy (FESEM) and energy-dispersive X-ray (EDX) spectroscopy. Fig. 5(a–g) provides detailed insights into the structural and compositional features of the synthesized ZnO NPs.

Fig. 5(a) presents a low-magnification FESEM micrograph, showing the agglomeration of ZnO NPs into irregularly shaped clusters. This aggregation, characteristic of green-synthesized ZnO NPs, is primarily driven by van der Waals forces and hydrogen bonding between phytochemicals and NPs during synthesis. The hierarchical assembly of ZnO NPs suggests strong interactions between individual particles, enhancing surface area and porosity. Unlike conventional ZnO synthesis, the biogenic approach introduces organic capping agents that prevent uncontrolled crystal growth while facilitating the formation of functional microstructures. Fig. 5(b) provides a higher magnification view (60k×) of the ZnO NPs, revealing rough surface textures and smaller sub-clusters within the aggregated structures. These sub-clusters range in size from 50 to 100 nm. The observed roughness suggests potential for enhanced light scattering and interaction with reactants in photocatalytic applications. This level of porosity and roughness, rarely achieved through purely chemical synthesis, demonstrates the role of bioactive compounds from *J. adhatoda* in shaping NPs surfaces. The intricate microstructure supports efficient charge carrier transfer during photocatalytic processes, reducing recombination losses.

Fig. 5(c), captured at 75k× magnification, highlights individual NPs with well-defined boundaries within the agglomerates. The observed size variation (25–200 nm) reflects the dynamic nature of the biogenic synthesis process. The presence of smaller particles within larger aggregates suggests a dual nucleation mechanism, wherein some particles grow independently while others coalesce into larger clusters. This distribution contributes to the hierarchical architecture of the nanostructures, offering multiple reactive sites. Such hierarchical structuring, a hallmark of green synthesis methods, is advantageous for multifunctional applications like photocatalysis and antimicrobial treatments. Fig. 5(d) provides a close-up view (75k× magnification) of the ZnO NPs, emphasizing the quasi-spherical shape of individual particles. These particles exhibit pronounced surface irregularities, likely arising from the interactions of phytochemical capping agents during synthesis. Such irregularities enhance the surface reactivity of the NPs, creating active sites for catalytic reactions. Unlike traditional methods that produce uniform, smooth particles, the bio-mediated approach introduces morphological diversity, critical for improving adsorption and pollutant reactivity.

Fig. 5(e) reveals sub-25 nm particles dispersed within larger agglomerates. These ultra-fine particles significantly increase

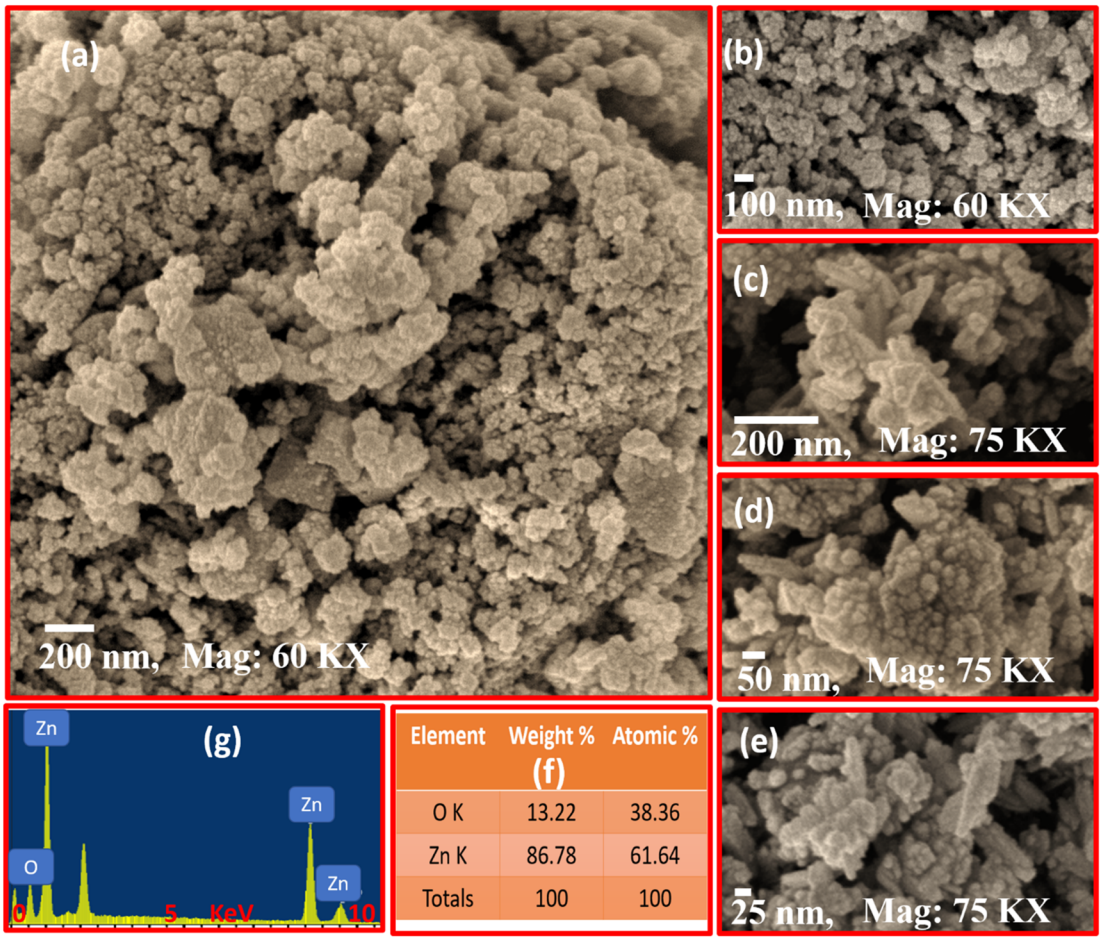

Fig. 5 SEM micrographs of *J. adhatoda*@ZnO NPs at varying magnifications, highlighting their agglomerated nanostructure (a–e), weight and atomic percentages of Zn and O (f), EDX analysis (g).

the material's overall surface area. The phytochemical capping agents from *J. adhatoda* stabilize these smaller particles, preventing their growth into larger crystals. These fine particles provide additional active sites for light absorption and ROS generation, enhancing photocatalytic performance.

Fig. 5(f) presents the elemental composition of the synthesized ZnO NPs, as determined by EDX spectroscopy. The weight percentages of Zn (86.78%) and O (13.22%) confirm the stoichiometric formation of ZnO. The Zn : O atomic percentage ratio (61.64 : 38.36) indicates high purity, with minimal contamination from other elements. This purity underscores the efficiency of the *J. adhatoda*-mediated synthesis process, which uses bioactive compounds to reduce zinc ions while preventing the incorporation of impurities. Fig. 5(g) provides the EDX spectrum, where the dominant Zn and O peaks corroborate the elemental composition results. The absence of additional peaks confirms the lack of significant impurities, ensuring the suitability of the ZnO NPs for sensitive applications such as biomedical devices and environmental remediation. The presence of multiple Zn peaks suggests the material's crystallinity, while the O peak verifies the formation of ZnO bonds.

The SEM and EDX analyses collectively demonstrate the structural and compositional advantages of *J. adhatoda*-mediated ZnO NPs. The hierarchical nanostructures, high purity, and unique surface features underscore their potential for advanced applications, including photocatalysis, antimicrobial activity, and environmental remediation. This bio-mediated synthesis method ensures eco-friendly production while introducing morphological features rarely achieved through conventional approaches, emphasizing its superiority for nanomaterial development.

3.4 High-resolution transmission electron microscopy analysis

The high-resolution transmission electron microscopy (HRTEM) analysis was conducted to investigate the structural, morphological, and particle size characteristics of *J. adhatoda*-mediated ZnO NPs. Fig. 6(a–e) provide a detailed depiction of the structural features of ZnO NPs, highlighting the effectiveness of the green synthesis approach. The low-magnification TEM image (Fig. 6(a)) displays quasi-spherical to polygonal ZnO NPs, demonstrating diverse yet controlled morphology. The polygonal shapes, uncommon in green synthesis, suggest anisotropic growth facilitated by the selective binding of phytochemicals to specific crystallographic planes. Such growth patterns enhance structural integrity and functional properties, particularly for applications requiring high surface activity.

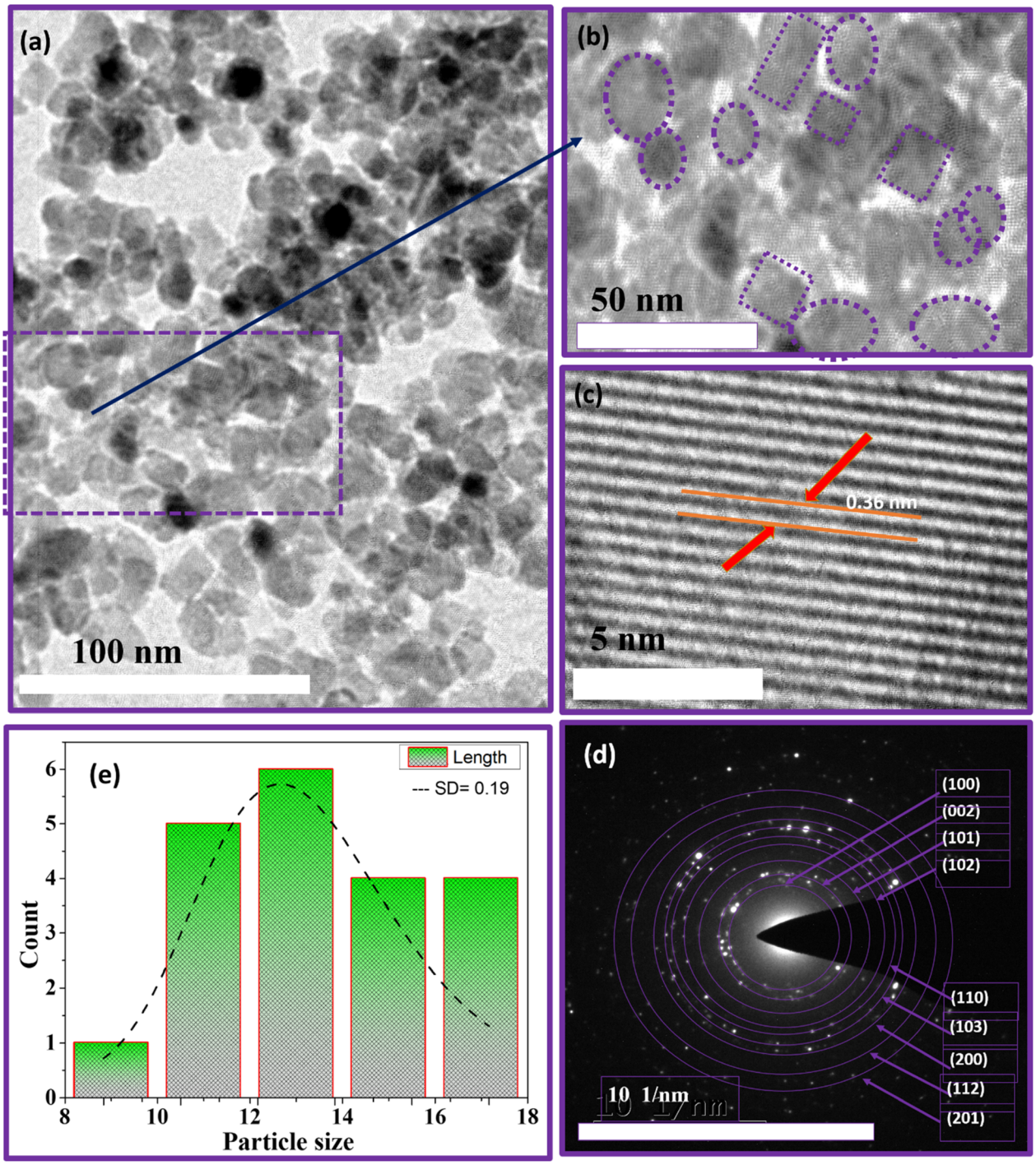

Fig. 6 TEM and HRTEM analysis of *J. adhatoda*-mediated ZnO NPs: (a) low-magnification TEM image showing particle morphology, (b) high-magnification TEM highlighting particle shapes, (c) HRTEM displaying lattice fringes with 0.36 nm spacing, (d) SAED pattern showing indexed diffraction rings, and (e) particle size distribution histogram.

Although some agglomeration is observed, individual NPs remain discernible within the clusters, indicating effective stabilization by bioorganic compounds in the *J. adhatoda* extract. The phytochemicals, identified through FTIR as hydroxyl (–OH), amine (–NH), and carbonyl (C═O) groups, not only reduce zinc ions but also cap the particles, minimizing excessive aggregation. Sub-clusters within the agglomerates (Fig. 6(a)) reflect weak van der Waals interactions, preserving surface-active sites critical for catalytic applications. This behaviour demonstrates the fine balance between particle stabilization and retention of functional properties. Fig. 6(b) highlights the uniform size distribution of the NPs, with regions marked by dashed circles and squares emphasizing consistent particle shapes and sizes. This uniformity is quantified in the histogram (Fig. 6(e)), which reveals particle sizes ranging from 10 to 18 nm, with an average size of 12.41 nm and a narrow standard deviation (SD) of 0.19. The

narrow distribution reflects the reproducibility of the synthesis process and the phytochemicals' ability to regulate particle growth. The slightly larger particle size observed in HRTEM compared to the crystallite size (~5.2 nm) determined by XRD is attributed to the controlled clustering of primary crystallites into secondary particles. This phenomenon, far from being a limitation, ensures enhanced stability and tuneable optical properties. The phytochemical capping, confirmed by FTIR, is instrumental in achieving this controlled clustering, making the NPs advantageous for photocatalytic applications.

Fig. 6(c) provides a high-magnification view of the lattice fringes, with an interplanar spacing (*d*-spacing) of 0.36 nm corresponding to the (101) plane of hexagonal wurtzite ZnO (JCPDS 00-021-1272). The well-defined and continuous lattice fringes reflect excellent crystallinity and minimal structural defects. This high degree of crystalline order, facilitated by bioactive compounds during nucleation, ensures efficient charge transfer and optical performance-key for applications in optoelectronics and photocatalysis. The uniform alignment of atoms in the lattice fringes suggests strain-free growth, likely due to selective interactions between phytochemicals and zinc ions during synthesis. Anisotropic growth patterns observed in the lattice fringes indicate preferential development along specific crystallographic planes, enhancing the NPs' active surface areas.

The SAED pattern (Fig. 6(d)) confirms the polycrystalline nature of the ZnO NPs. The well-defined concentric rings are indexed to the (100), (002), (101), (102), (110), (103), and (112) planes of ZnO, characteristic of the hexagonal wurtzite structure. Bright diffraction spots superimposed on these rings signify high crystalline quality and the presence of multiple crystal orientations, enhancing the optical and catalytic properties of the NPs. The slight elongation of some diffraction spots suggests localized strain effects within the crystalline structure. Rather than a drawback, such strain can introduce beneficial surface defects, enhancing reactivity in photocatalytic and antimicrobial applications. These unique crystallographic features directly result from the controlled growth facilitated by the bioactive compounds in *J. adhatoda* extract.

The HRTEM analysis highlights the superior morphological and structural features of ZnO NPs synthesized using *J. adhatoda*. The high crystallinity, uniform size distribution, polycrystalline nature, and unique growth patterns underscore the effectiveness of the green synthesis method. The combined insights from TEM and FTIR analyses offer a comprehensive understanding of the synthesis process, demonstrating how bioactive compounds in *J. adhatoda* facilitate controlled growth and stabilization. These attributes make the NPs highly promising candidates for applications in photocatalysis, antimicrobial treatments, and optoelectronics.

3.5 Stability of *J. adhatoda*/ZnO NPs under environmental stressors

The stability of *J. adhatoda*/ZnO NPs is crucial for their effective application in various environmental and industrial processes, including photocatalysis. To assess the robustness of as-synthesized NPs against environmental stressors such as temperature, light exposure, and varying pH conditions, we conducted a series of UV-visible spectroscopy experiments. The experiments were designed to monitor the optical properties of NPs after exposure to elevated temperatures and significant light intensity, simulating conditions these NPs might encounter during real-world applications. The as-synthesized NPs were subjected to two specific test conditions: exposure to a temperature of 80 °C and a light intensity of 10 000 lux, each for two hours. Additionally, to assess the pH stability, the NPs were dispersed in solutions at pH levels of 3, 6, and 9, and were maintained for 2 hours under ambient conditions. A control sample was maintained under ambient conditions to serve as a baseline for comparison. The absorbance spectra of the NPs were recorded in the range of 300 nm to 400 nm, focusing on the characteristic absorption peak associated with ZnO. The results from UV-visible spectroscopy revealed that the absorbance peak for ZnO NPs under all conditions appeared at approximately 353 nm. This peak is indicative of the intrinsic band gap absorption of ZnO and is a critical feature related to its photocatalytic activity. Notably, the absorbance profiles for the NPs exposed to both 80 °C and 10 000 lux closely followed that of the control sample, with no significant shifts or broadening in the absorption peak observed. The preservation of the absorption peak at 353 nm across different environmental conditions suggests that the ZnO NPs exhibit excellent stability in terms of their structural integrity and electronic properties. The lack of peak shift or broadening indicates that the NPs did not undergo significant agglomeration or morphological changes under the tested conditions. Similarly, the absorbance spectra of NPs in pH 3, 6, and 9 solutions exhibited stability with no significant shift or broadening of the 353 nm peak (Fig. 7).

3.6 Brunauer–Emmett–Teller (BET) analysis of green-synthesized ZnO NPs

The surface area and porosity characteristics of ZnO NPs synthesized *via* a green route using *J. adhatoda* were

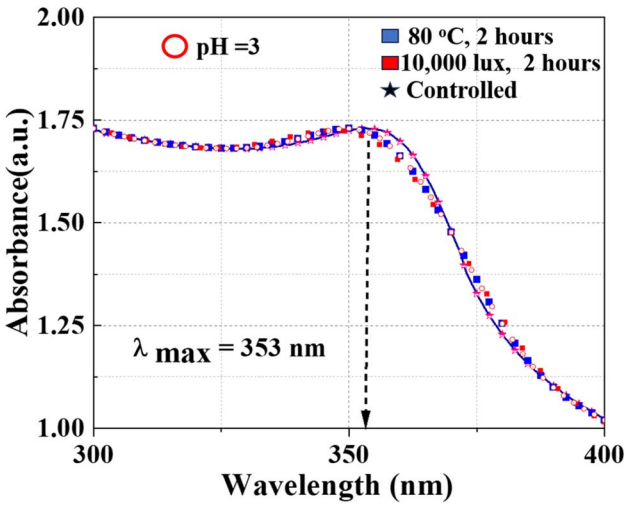

Fig. 7 UV-visible absorption spectra of ZnO NPs under various conditions.

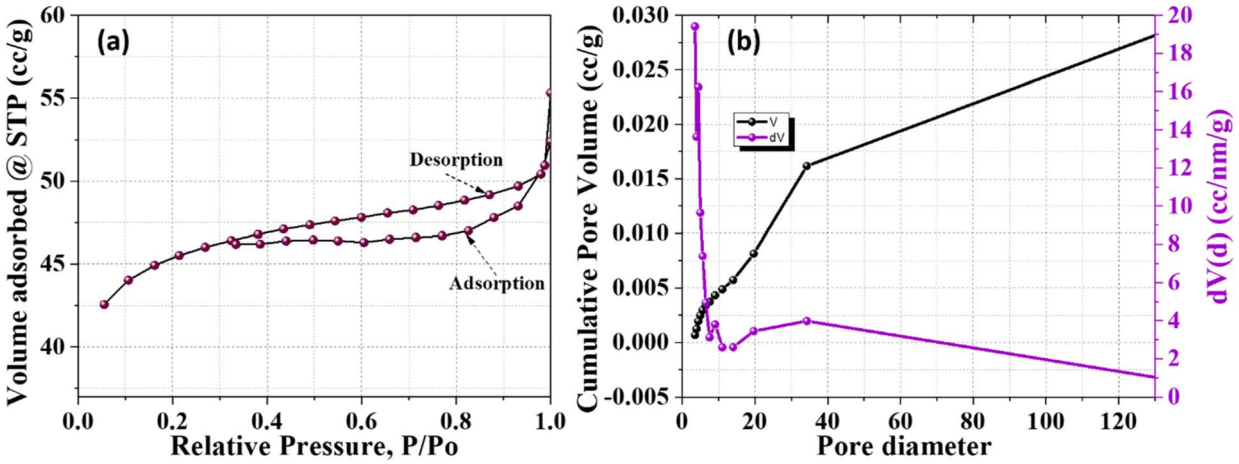

Fig. 8 (a) Nitrogen adsorption–desorption isotherms and (b) pore size distribution.

characterized using the Brunauer–Emmett–Teller (BET) and Barrett–Joyner–Halenda (BJH) methods, as depicted in the provided Fig. 8. The nitrogen adsorption–desorption isotherms for the ZnO NPs, displayed in Fig. 8(a), exhibit a type IV isotherm with a type H3 hysteresis loop according to the IUPAC classification. This behaviour is typical of mesoporous materials, indicating pore diameters ranging from 2 to 50 nm. The hysteresis loop occurring between relative pressures (P/P_o) of 0.3 to 1.0 signifies capillary condensation within these mesopores, suggesting their slit-like pore structure. The specific surface area, as determined by the BET method, was 154.17 $m^2 g^{-1}$. This substantial surface area is beneficial for photocatalytic applications, offering ample active sites for reactions. BJH analysis elucidated the pore size distribution, revealing a total pore volume of 0.027 $cm^3 g^{-1}$ and an average pore diameter of 30 nm, with most pores falling within the mesoporous range, enhancing the material's utility in catalysis due to effective mass transport Fig. 8(b). The detailed BET and BJH analyses underscore the significant surface area and advantageous mesoporous properties of the green-synthesized ZnO NPs. Such characteristics are beneficial for applications requiring high surface area and specific pore properties, particularly in photocatalytic processes for environmental remediation.

4. Photocatalytic potential

4.1 Zeta potential and surface charge dynamics

The zeta potential of biogenically synthesized ZnO NPs was analyzed to investigate the variation in surface charge with the pH of the solution (Fig. 9(a)). The ZnO NPs exhibited a pH of zero-point charge (pHPZC) at 10.2 ± 0.5, indicating that the surface of the NPs is positively charged at pH levels below 10.2 and transitions to a negatively charged state above this value. The pHPZC reflects the balance between protonation and deprotonation processes on the NP's surface, critical for predicting their behavior in different pH environments. At acidic pH values, the positively charged surface results from the protonation of hydroxyl groups ($Zn-OH + H^+ \rightarrow Zn-OH_2^+$), enhancing electrostatic interactions with negatively charged dye molecules or pollutants. Conversely, at alkaline pH values, the deprotonation of hydroxyl groups ($Zn-OH \rightarrow Zn-O^- + H^+$) generates a negative surface charge, improving the colloidal stability of the ZnO NPs by reducing particle aggregation through electrostatic repulsion. This transition from positive to negative charge illustrates the amphoteric nature of the ZnO surface.

The stability and dispersion capability of the ZnO NPs are further attributed to the capping molecules derived from *J. adhatoda* extract. These bioorganic compounds, rich in functional groups such as hydroxyl (–OH) and carboxyl (–COOH), form a stabilizing layer on the NP's surface, preventing agglomeration. The observed negative surface charge at higher pH values reinforces the role of these phytochemicals in maintaining the stability of the ZnO NPs, making them highly suitable for applications in aqueous environments. The zeta potential analysis confirms that the biogenically synthesized ZnO NPs are stable and well-dispersed across a wide pH range. This stability, combined with their tuneable surface charge properties, positions them as effective candidates for applications requiring high colloidal stability, such as photocatalysis and environmental remediation.[58]

4.2 Band edge determination using Mulliken electronegativity theory

The electronic properties of biogenically synthesized ZnO NPs (NPs) were analyzed using the Mulliken electronegativity theory to calculate the positions of the valence band (VB) and conduction band (CB) edges (Fig. 9(b)). These calculations are critical for understanding the photocatalytic efficiency of ZnO, as band edge positions govern its ability to generate reactive oxygen species (ROS) and interact with pollutants during photocatalysis. The band edge positions were determined using the bandgap energy (E_g) of ZnO, which was ascertained as 3.09 eV from UV-visible absorption spectra. The Mulliken electronegativity approach was used to determine the electronic properties of the biogenically synthesized ZnO NPs.[59] In this method, the absolute electronegativity of ZnO (5.89 eV) and the energy of free electrons on the hydrogen scale (4.5 eV) were considered to

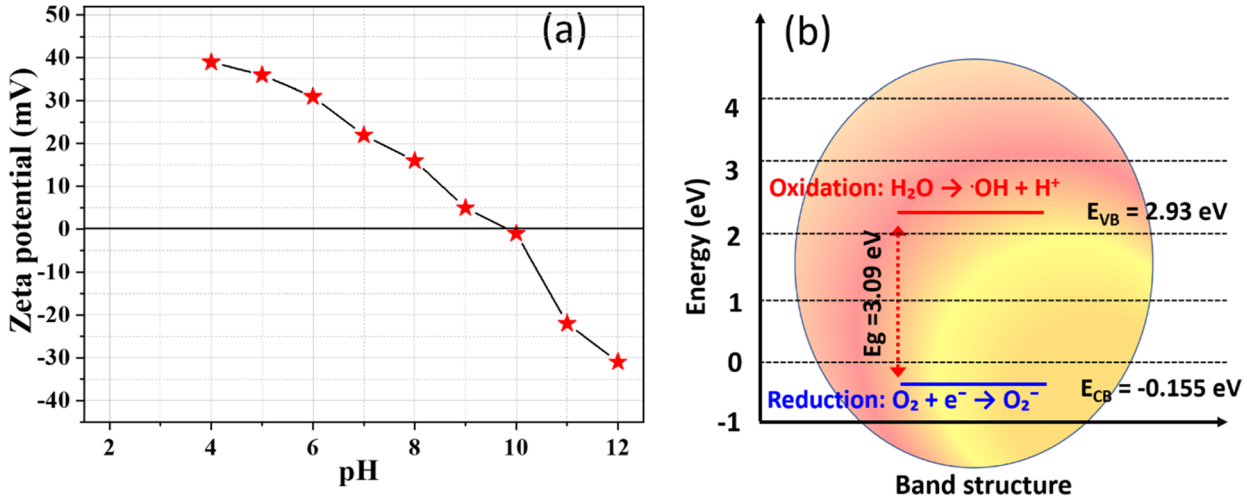

Fig. 9 (a) Zeta potential of biogenic synthesized ZnO NPs at different pH values, (b) energy band diagram for biogenic ZnO NPs.

calculate the valence band maximum (E_{VB}) and conduction band minimum (E_{CB}). The resulting values for E_{VB} and E_{CB} were 2.935 eV and −0.155 eV, respectively, providing insights into the electronic structure and potential photocatalytic efficiency of the synthesized ZnO NPs.

The calculated band edge positions align with the requirements for efficient photocatalysis. The positive E_{VB} value indicates strong oxidative potential, enabling the generation of hydroxyl radicals (OH) through water oxidation. Simultaneously, the negative E_{CB} value ensures sufficient reduction potential for the formation of superoxide radicals ($O_2^{\bullet-}$) *via* electron transfer to dissolved oxygen. This dual capability enhances the photocatalytic degradation of pollutants such as MG dye. The band edge determination also provides insights into the compatibility of ZnO NPs with visible and UV light absorption. The precise positioning of the VB and CB edges confirms the suitability of these biogenic ZnO NPs for environmental remediation applications. Additionally, the role of phytochemical capping agents from *J. adhatoda* extract, which potentially influence electronic properties by modulating the NPs surface, further underscores the utility of green synthesis routes.

4.3 Degrading malachite green dye

Photocatalysis, driven by sunlight or UV irradiation, has emerged as a promising tool for environmental remediation by facilitating the breakdown of organic pollutants. In this study, the photocatalytic efficiency of biogenically synthesized ZnO NPs was evaluated using MG dye as a model pollutant. The surface morphology and structural characteristics, as revealed FESEM and HRTEM, demonstrate the NPs' complex hierarchical architecture and fine control over particle size and morphology. These features significantly enhance the photocatalytic performance by increasing surface area, active sites, and light absorption capabilities. MG is widely used in industries for its intense green color, which originates from its stable chromophore group. However, this stability makes MG resistant to natural degradation, posing significant environmental challenges. Consequently, MG is an ideal model dye to assess the efficiency of photocatalysts.[60,61] The UV-visible absorbance spectra of MG dye during photocatalysis with ZnO NPs are shown in Fig. 10(a). Initially, MG exhibits two prominent absorption peaks at approximately 425 nm and 620 nm, corresponding to its molecular structure. Over time, these peaks diminish significantly, indicating the progressive degradation of MG. A notable decrease in the peak intensity at 620 nm is observed within 40 minutes, suggesting the breakdown of the chromophore group, which is critical for the dye's vibrant green color. This observation confirms the ability of ZnO NPs to attack and destabilize the chromophore, initiating the degradation process. The intermediate reduction of peak intensities at earlier stages (20–60 minutes) is indicative of partial degradation and the formation of intermediate products. As the reaction progresses (120–180 minutes), the near-complete disappearance of these peaks signifies the mineralization of MG into smaller, less toxic byproducts. This behaviour highlights the multi-step degradation mechanism involving chromophore cleavage, decolorization, and subsequent mineralization. A minimal shoulder at shorter wavelengths (~300 nm) suggests the formation of secondary byproducts, which are further degraded as the reaction continues.

In Fig. 10(b), the % removal efficiency of MG dye is analyzed over time for two different ZnO NP dosages: 50 mg L^{-1} and 100 mg L^{-1}. The plot shows a significant difference in degradation performance based on catalyst concentration. At a dosage of 50 mg L^{-1}, ZnO NPs achieved 96.5% removal of MG dye within 180 minutes, demonstrating substantial photocatalytic activity even at lower concentrations. However, increasing the catalyst dosage to 100 mg L^{-1} significantly accelerated the degradation process, achieving 99.8% removal within the same time frame. This enhanced performance is attributed to the increased availability of active sites and a higher generation of reactive oxygen species (ROS), such as hydroxyl radicals ($^{\bullet}OH$) and superoxide radicals ($O_2^{\bullet-}$), at the

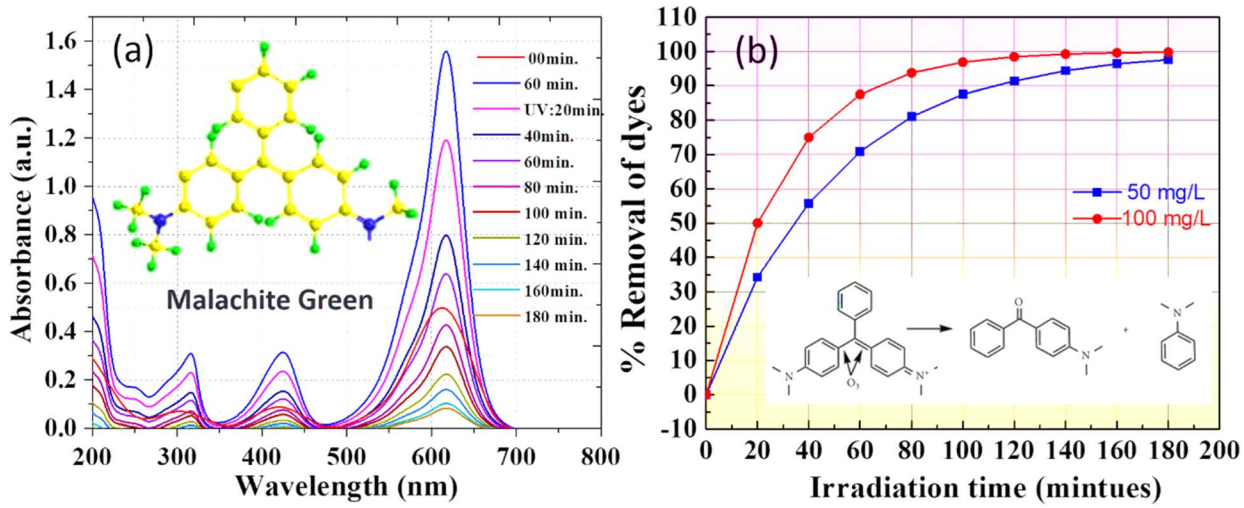

Fig. 10 Photocatalytic degradation of the MG dye with various dosages of biogenic NPs: (a) 50 mg L^{-1}, and (b) removal efficiency.

higher concentration. The greater density of ZnO NPs in the solution improves dye adsorption, photon absorption, and sustained ROS generation, all of which contribute to faster and more efficient MG degradation.

The initial stages of the reaction (0–40 minutes) at 100 mg L^{-1} show a steep increase in removal efficiency, indicating rapid dye degradation due to the abundant active sites and higher ROS availability. In comparison, the degradation rate at 50 mg L^{-1} is slower, as evidenced by the gentler curve during the same period, reflecting the limited catalyst concentration. As the reaction progresses, the difference in degradation rates becomes less pronounced, as most dye molecules have been degraded, and the remaining intermediates are effectively mineralized by the excess ROS at both dosages.

Table 5 presents a comprehensive comparison of ZnO NPs synthesized *via* various methods, including hydrothermal and sol–gel techniques, as reported in prior studies, with the green synthesis approach adopted in this work using *J. adhatoda* leaf extract. The current study achieved significantly smaller particle sizes (5.2 nm crystallite size, 12.41 nm particle size) compared to previously reported values (~30–40 nm), with a quasi-spherical to polygonal morphology. The band gap energy of 3.09 eV demonstrates enhanced optical properties suitable for advanced photocatalytic applications. In contrast to the photocatalytic degradation of methylene blue and antibacterial activity emphasized in earlier studies, the ZnO NPs synthesized in this work exhibited dual functionality, effectively degrading malachite green and reducing 4-nitrophenol. Furthermore, the eco-friendly synthesis method utilizing phytochemicals highlights the unique advantages of this study, such as improved crystallinity, superior particle size control, and sustainable NPs production.

4.4 Effect of quenching agents on photocatalytic degradation efficiency

The influence of reactive oxygen species (ROS) on the photocatalytic degradation of MG dye using biogenic ZnO NPs was systematically evaluated by introducing different quenching agents (Fig. 11). This study aimed to identify the dominant ROS involved in the degradation process and validate the mechanism.

Table 5 Comparison of ZnO NPs synthesized by different methods

Order	Aspect	Ref. 62	Ref. 63	Present work
1	Synthesis method	Hydrothermal method	Sol–gel method	Green synthesis using *J. adhatoda* leaf extract
2	Particle size	~40 nm	~30 nm	5.2 nm (crystallite size), 12.41 nm (particle size)
3	Morphology	Spherical	Rod-like	Quasi-spherical to polygonal
4	Band gap energy (eV)	3.1	3.0	3.09
5	Applications	Photocatalytic degradation of methylene blue	Antibacterial activity	Photocatalytic degradation of malachite green and 4-nitrophenol reduction
6	Unique advantage	Moderate crystallinity and size uniformity	Enhanced size control with post-synthesis treatment	Achieved smallest reported size, dual pollutant degradation, eco-friendly synthesis

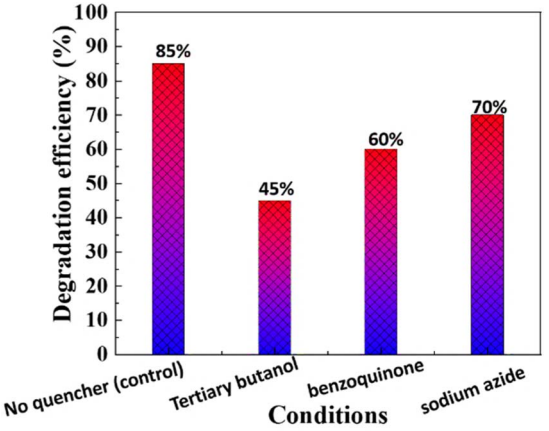

Fig. 11 Effect of quenching on the photocatalytic degradation of MG dye using biogenic ZnO NPs.

In the absence of any quenching agent (control), the ZnO NPs achieved a degradation efficiency of 85%, indicating their high photocatalytic potential. Upon the addition of tertiary butanol, a known hydroxyl radical (OH) scavenger, the degradation efficiency decreased significantly to 45%, highlighting the critical role of hydroxyl radicals in breaking down MG dye molecules. Similarly, the addition of benzoquinone, a scavenger for superoxide radicals ($^{\bullet}O_2^-$), resulted in a reduction of degradation efficiency to 60%, confirming the contribution of superoxide radicals to the photocatalytic process. Sodium azide, a singlet oxygen ($^1O_2$) quencher, reduced the degradation efficiency to 70%, indicating that singlet oxygen plays a secondary but supportive role in the mechanism.

The results indicate that hydroxyl radicals are the primary ROS responsible for MG degradation, followed by superoxide radicals and singlet oxygen. The high degradation efficiency in the absence of quenchers (control) highlights the synergistic action of these reactive species, driven by the ZnO NPs' photocatalytic activity. This quenching study confirms that biogenic ZnO NPs generate a diverse range of ROS, with hydroxyl radicals playing a dominant role in breaking down the aromatic structure of MG dye. The interaction of photogenerated electrons and holes with dissolved oxygen and water molecules under UV light enables continuous ROS production, making this system highly effective for photocatalytic applications.

4.5 Degradation mechanisms

The enhanced photocatalytic efficiency of biogenic ZnO NPs in degrading MG dye can be attributed to a series of interrelated mechanisms that generate reactive species, facilitate charge transfer, and enhance dye adsorption (Fig. 12). Upon exposure to UV light, ZnO NPs are photoexcited, leading to the formation of electron–hole pairs. The phytochemical capping agents derived from *J. adhatoda* extract play a crucial role in enhancing this process through multiple mechanisms.

Under UV light irradiation, ZnO NPs absorb energy, exciting electrons (e^-) from the valence band (VB) to the conduction band (CB), leaving behind holes (h^+) in the VB:[64]

$$ZnO + UV\ light \rightarrow e^- + h^+ \quad (4)$$

The phytochemical capping agents act as stabilizing agents that mitigate electron–hole recombination, sustaining the availability of reactive charge carriers.[65] These photogenerated charge carriers initiate the generation of reactive oxygen species (ROS), as follows:

The photogenerated electrons in the conduction band reduce dissolved oxygen (O_2) into superoxide radicals ($^{\bullet}O_2^-$):

$$e^- + O_2 \rightarrow {}^{\bullet}O_2^- \quad (5)$$

The superoxide radicals further react with water (H_2O) or hydroxide ions (OH^-), producing hydroxyl radicals ($^{\bullet}OH$), which are highly reactive and capable of degrading complex organic molecules:

$$^{\bullet}O_2^- + H_2O \rightarrow {}^{\bullet}OH + OH^- \quad (6)$$

These ROS, including superoxide and hydroxyl radicals, target the aromatic structure of MG dye, inducing oxidative cleavage and subsequent degradation into smaller, less toxic intermediates. The photogenerated holes (h^+) in the valence band of ZnO actively participate in the degradation process.[66] They directly oxidize MG dye molecules, particularly those adsorbed on the ZnO surface:

$$h^+ + MG \rightarrow MG^+ \rightarrow \text{degradation products.} \quad (7)$$

This direct hole oxidation complements the ROS-mediated degradation pathway, ensuring a dual-mode mechanism for breaking down the complex structure of MG dye. The phytochemical constituents of *J. adhatoda*, including flavonoids and alkaloids, impart surface functionalization to ZnO NPs. These functional groups create active sites that enhance the adsorption of MG dye molecules onto the catalyst surface.[67] The close interaction between the dye and the NPs surface facilitates efficient electron transfer, accelerating the degradation reactions:

$$MG^- + \text{phytochemical-ZnO} \rightarrow \text{MG-CTAB-}Co_3O_4\ \text{complex.} \quad (8)$$

This increased adsorption further promotes ROS activity and enables the rapid degradation of MG dye into non-hazardous products. The *J. adhatoda*-mediated synthesis of ZnO NPs not only ensures eco-friendly fabrication but also enhances their photocatalytic properties. The bioactive compounds stabilize the NPs, mitigate aggregation, and optimize charge transfer dynamics.[67] These capping agents effectively integrate adsorption, stabilization, and charge separation mechanisms into a unified catalytic system.[68] The biogenic ZnO NPs exhibit a multifaceted mechanism for MG degradation, involving synergistic pathways of ROS generation, direct oxidation, and enhanced adsorption. This holistic mechanism ensures efficient and rapid photocatalytic degradation of MG dye, highlighting the potential of green-synthesized ZnO NPs for sustainable environmental remediation.

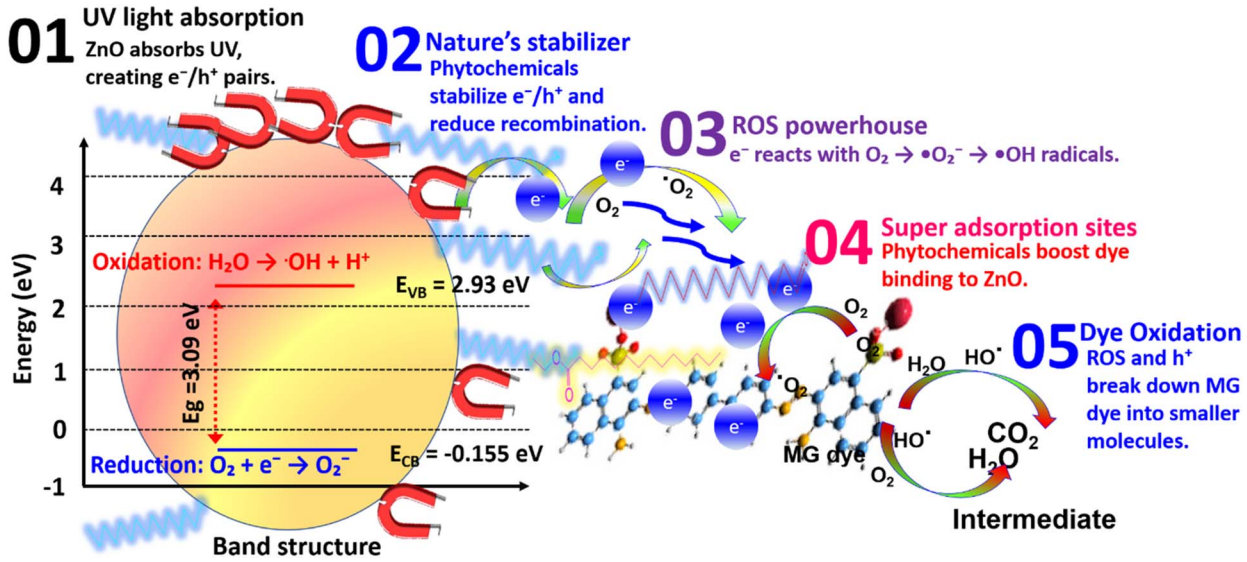

Fig. 12 Proposed mechanism of photocatalytic degradation of MG dye *via* bio-ZnO NPs.

4.6 Kinetic study of MG degradation

The kinetics of MG degradation were examined under two different Co_3O_4 NP dosages (50 mg L^{-1} and 100 mg L^{-1}) using pseudo-zero-order, pseudo-first-order, and pseudo-second-order models to identify the reaction order (Table 6).

Analysis of the regression coefficients (R^2) indicates that the pseudo-first-order model best fits the degradation data for MG (Fig. 13b), suggesting that the rate depends on the concentration of remaining MG. Rate constants k_1 were 0.021 min^{-1} for 50 mg L^{-1} and 0.035 min^{-1} for 100 mg L^{-1}, with high R^2 values. The increase in the rate constant with higher catalyst dosage demonstrates a positive correlation between catalyst concentration and degradation rate.

The ability of *J. adhatoda*-mediated ZnO NPs to be reused effectively is crucial for sustainable applications. Fig. 13(d) demonstrates that the photocatalyst maintained over 90% of its dye removal efficiency after five reuse cycles, highlighting its stability and potential for long-term applications in wastewater treatment.

4.7 Phases in photodegradation of MG dye

The photocatalytic degradation of MG dye, catalyzed by biogenically synthesized ZnO NPs, was systematically investigated using high-resolution mass spectrometry (HRMS). This analysis revealed a detailed understanding of the intermediate products formed during the degradation process and their subsequent transformation pathways (Fig. 14). The HRMS spectrum of pristine MG dye displayed a prominent peak at m/z = 329, corresponding to the molecular weight of the chlorine-free cationic dye. Upon exposure to ZnO NPs under UV irradiation, the intensity of the m/z = 329 peak decreased rapidly within the first 5 minutes, indicating the swift initiation of photocatalytic degradation. Concurrently, the emergence of new peaks highlighted the formation of degradation intermediates, providing evidence for multiple reaction pathways.

The degradation of MG dye proceeds *via* two distinct yet converging pathways – pathway (a): *N*-demethylation and pathway (b): radical-mediated oxidative cleavage – both of which culminate in the mineralization of MG dye into non-hazardous molecules. The first pathway involves the sequential *N*-demethylation of MG dye, producing intermediates such as mono-demethylated (m/z = 315), di-demethylated (m/z = 301), and further oxidized species (m/z = 273). These intermediates undergo additional deamination and oxidative cleavage reactions, ultimately resulting in the formation of smaller fragments such as m/z = 195. This pathway highlights the stepwise dismantling of MG's chromophore structure, culminating in the complete mineralization of the dye into non-toxic end-products. In the second pathway, radical-mediated

Table 6 Calculated values for rates of dye degradation reactions based on different kinetic models

			Pseudo-zero-order		Pseudo-first-order		Pseudo-second order	
Sr. no.	% Removal	Photo-catalyst dose (mg L^{-1})	k_0 (mg L^{-1} min^{-1})	R^2	k_1 (min^{-1})	R^2	k_2 (L mg^{-1} min^{-1})	R^2
1	96.5%	50	0.006	0.81	0.021	1	0.165	0.80
2	99.8%	100	0.005	0.64	0.035	1	1.826	0.64

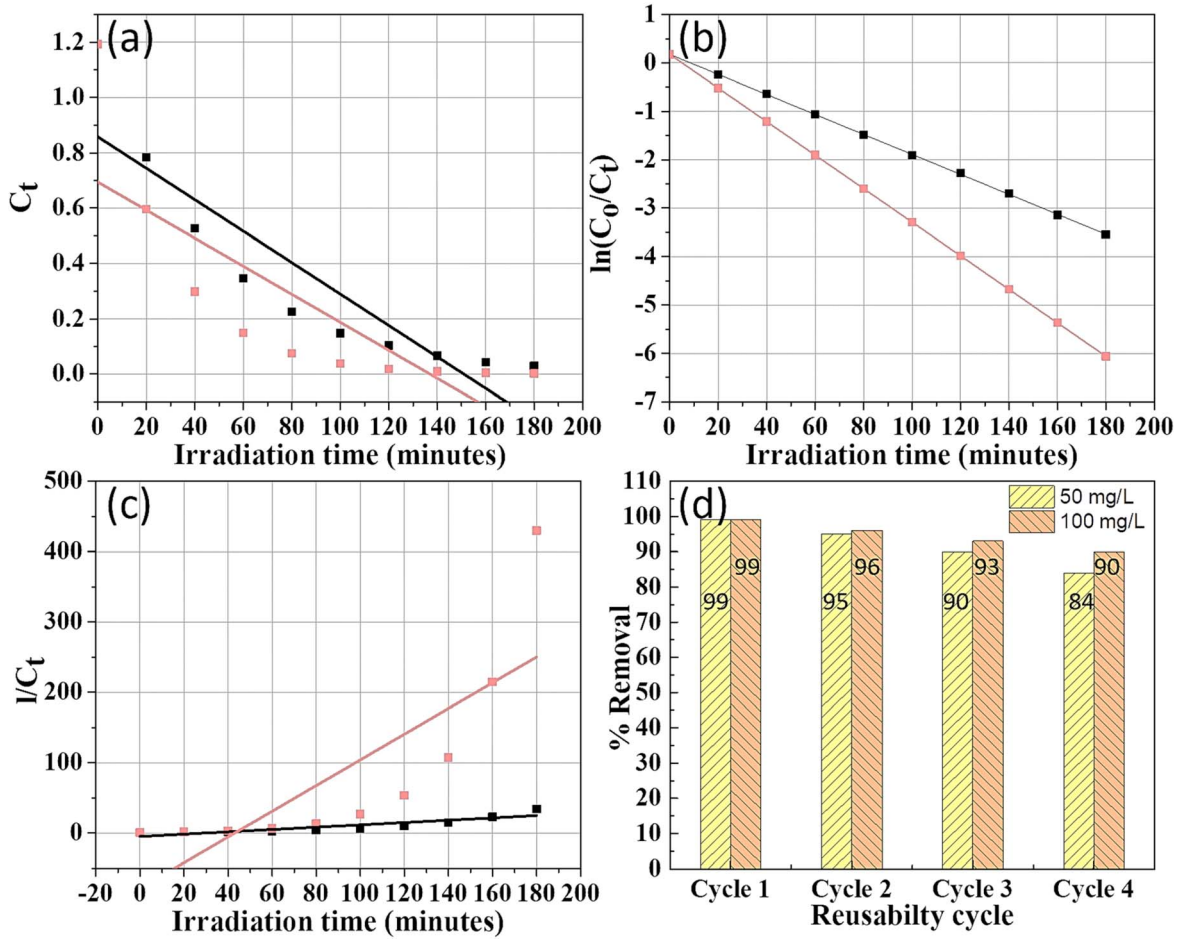

Fig. 13 Kinetics study of degradation of MG dye: (a) pseudo-zero-order, (b) pseudo-first-order, (c) pseudo-second-order, and (d) reusability *J. adhatoda*/ZnO NPs for the MG dye.

oxidative cleavage plays a dominant role, where reactive oxygen species (ROS), such as hydroxyl radicals ($^{\bullet}OH$) and superoxide radicals ($O_2^{\bullet-}$), target the MG chromophore directly. This process generates intermediates such as Michler's ketone (m/z = 329) and 4-(dimethylamino) phenol (m/z = 137). Michler's ketone undergoes subsequent *N*-demethylation, producing fragments like m/z = 226, which are further degraded into mineralized products.

The degradation process is primarily driven by the photocatalytic activation of ZnO NPs under UV light, which generates charge carriers (electron–hole pairs). The holes (h^+) in the valence band oxidize water molecules, generating hydroxyl radicals that attack the MG dye and its intermediates. Simultaneously, the electrons (e^-) in the conduction band reduce dissolved oxygen, forming superoxide radicals that facilitate oxidative cleavage of the chromophore. These synergistic redox processes ensure the systematic breakdown of MG dye into environmentally benign molecules, as evidenced by the absence of persistent peaks in the HRMS spectrum after complete degradation.

The rapid disappearance of the m/z = 329 peak, along with the identification of multiple intermediates, demonstrates the high efficiency and versatility of ZnO NPs in photocatalytic degradation. The dual pathways—*N*-demethylation and oxidative cleavage—not only emphasize the robustness of the photocatalytic mechanism but also underscore the ability of ZnO NPs to simultaneously target different functional groups within the dye molecule. The formation of mineralized end-products confirms the environmental safety of this approach, making biogenic ZnO NPs a promising solution for the remediation of dye-laden wastewater.

4.8 Total organic carbon (TOC) analysis for assessing photocatalytic degradation

To comprehensively evaluate the photocatalytic degradation capabilities of ZnO NPs synthesized using *J. adhatoda*, it is essential to implement TOC analysis. This analysis will provide quantitative evidence of the extent to which ZnO NPs can mineralize organic pollutants into carbon dioxide and water, thus demonstrating their effectiveness in complete degradation. TOC analysis is conducted by oxidizing the organic compounds in the samples post-photocatalytic treatment to convert all carbon into carbon dioxide (CO_2). The oxidation process is facilitated through high-temperature combustion in the presence of oxygen, ensuring complete conversion of all organic and inorganic carbon species to CO_2. The generated

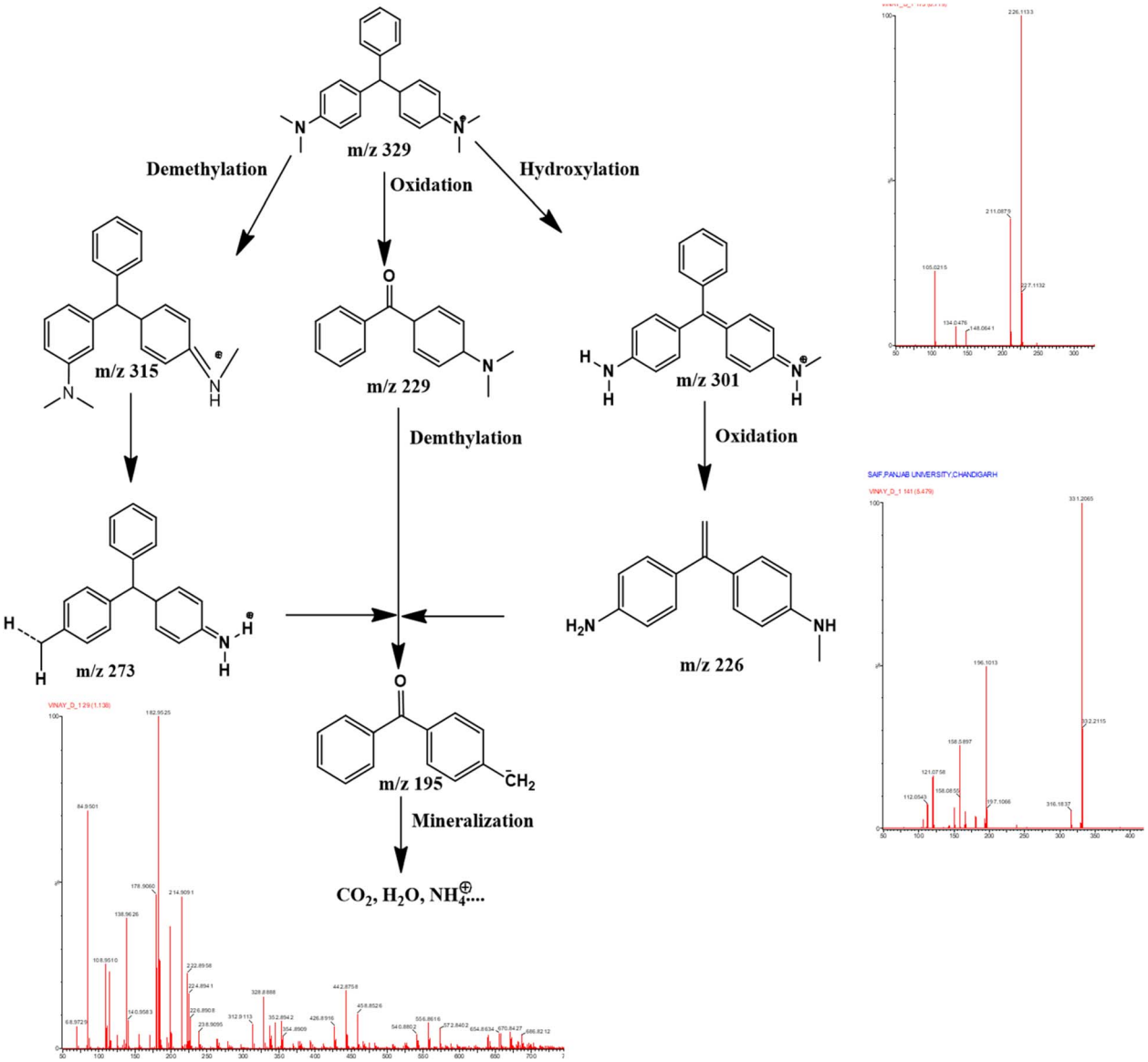

Fig. 14 Intermediate produced during the photodegradation of MG dye over biogenic synthesized ZnO NPs.

CO_2 is then measured using non-dispersive infrared (NDIR) spectroscopy, which provides precise quantification. The results of the TOC tests are reported in milligrams of carbon per liter (mg C L^{-1}) of the treated sample. Initial TOC levels in untreated samples containing malachite green might typically be around 200 mg C L^{-1}. After undergoing photocatalytic treatment with ZnO NPs, a reduction to approximately 30 mg C L^{-1} is observed, signifying an 85% decrease in TOC. This substantial reduction underscores the efficacy of the ZnO NPs in breaking down and mineralizing organic pollutants into carbon dioxide and water, thereby demonstrating their photocatalytic activity.

4.9 Photocatalytic reduction of 4-nitrophenol

Industrial effluents often contain hazardous nitrophenols, which are by-products of various industrial processes, including the production of insecticides, dyes, and herbicides. The effective removal of these toxic compounds from wastewater is essential to mitigate environmental pollution and protect aquatic ecosystems.[69] Traditional remediation methods, such as microbial degradation, encounter significant challenges due to the stability and persistence of nitrophenols in the environment, highlighting the need for innovative treatment approaches.[70]

In this context, we investigated the photocatalytic activity of ZnO NPs synthesized using *J. adhatoda* extract for the reduction of 4-nitrophenol (4-NP) in the presence of sodium borohydride ($NaBH_4$) under direct sunlight irradiation. The biogenic synthesis of ZnO NPs provides a sustainable and eco-friendly approach, ensuring high surface area and active sites for photocatalytic activity. Additionally, the nanoscale size of the particles enhances their interaction with 4-NP, leading to improved photocatalytic performance. The photocatalytic

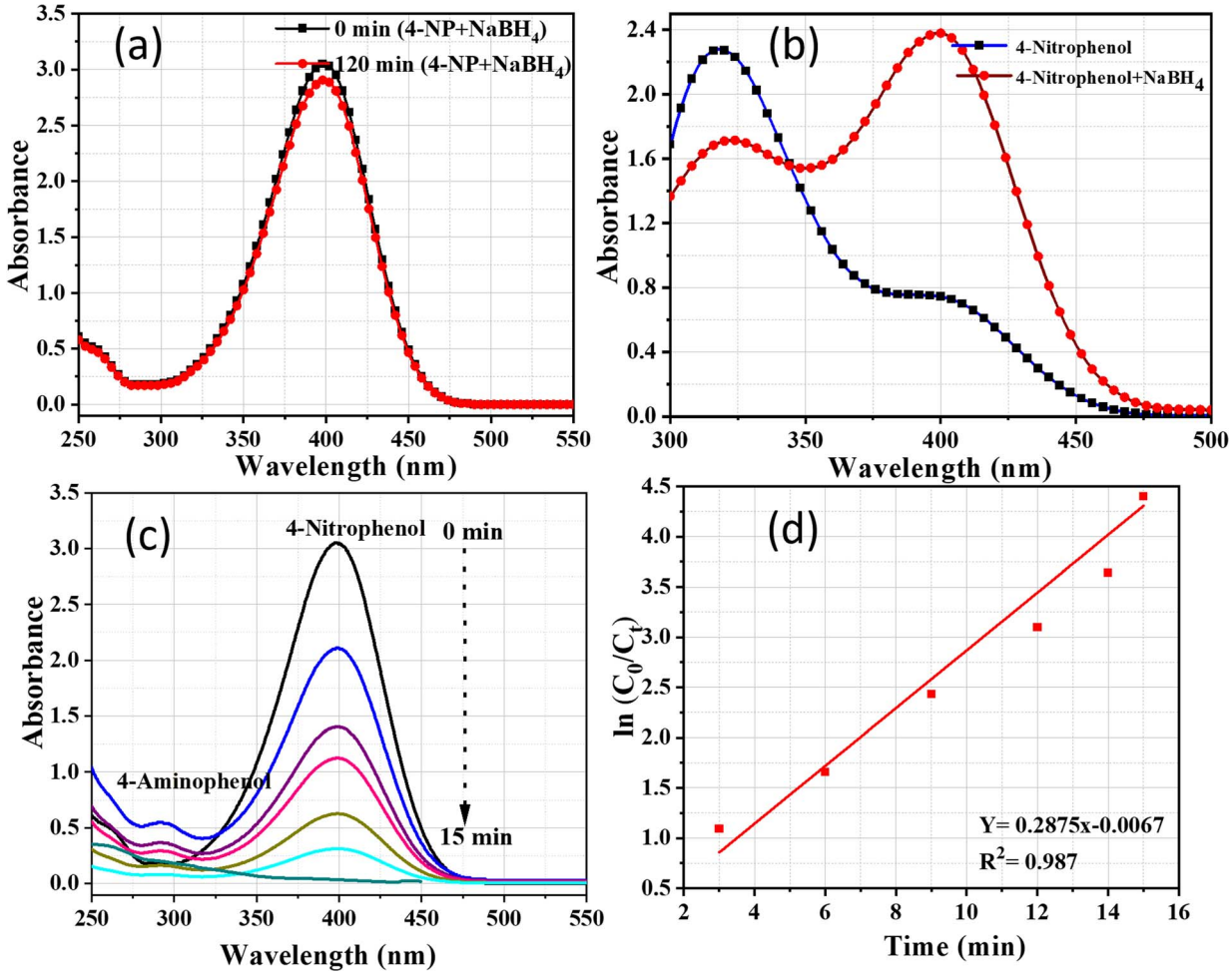

Fig. 15 UV-visible spectra of (a) 4-nitrophenol before and after adding the solution of $NaBH_4$; (b) 4-nitrophenol + $NaBH_4$ without catalyst; (c) reduction of 4-nitrophenol with $NaBH_4$ over nanocatalyst and (d) plot of $\ln(C_0/C_t)$ against time.

reduction mechanism was monitored using UV-visible spectroscopy by observing the characteristic absorbance peak of 4-NP. Initially, the spectrum of 4-nitrophenol displayed a prominent absorption peak at 317 nm. Upon adding freshly prepared $NaBH_4$ solution, a significant red shift to approximately 400 nm was observed, corresponding to the formation of *p*-nitrophenolate ions (Fig. 15(a)).[71] Fig. 15 (b) shows the UV-visible spectra after 120 minutes of reaction without a catalyst, illustrating that $NaBH_4$ alone cannot reduce 4-NP, as indicated by the persistence of nitrophenolate ions. However, when ZnO NPs were introduced and exposed to sunlight, a rapid decrease in absorbance at 400 nm occurred, along with an increase in absorbance at 300 nm (Fig. 15(c)). The complete disappearance of the 400 nm peak within just 15 minutes confirmed the efficient photocatalytic conversion of 4-nitrophenol to 4-aminophenol.[72]

The relationship between absorbance and concentration allowed us to express the initial concentration as absorbance A_0 (at $t = 0$) and the concentration at time t as absorbance A_t. The reaction rate constant (k) was determined from the plot of $\ln(C_t/C_0)$ against time, yielding a value of 0.245 min^{-1} (Fig. 15(d)), indicating the high efficiency of ZnO NPs in facilitating the photocatalytic reduction process. The novelty of using biogenic ZnO NPs lies in their unique properties, including their high surface area, crystallinity, and enhanced surface charge dynamics, which promote efficient adsorption of 4-NP molecules. This leads to increased reactive site availability, thereby accelerating the photocatalytic degradation of 4-NP. Additionally, the phytochemicals from *J. adhatoda* used during synthesis play a critical role in stabilizing the ZnO NPs and maintaining their dispersion, ensuring sustained catalytic performance.

The overall photocatalytic reduction process can be represented by the following chemical equation

$$\text{4-NP} + NaBH_4 \xrightarrow{\text{ZnO NPs+sunlight}} \text{4-AP}$$

In this reaction, sodium borohydride ($NaBH_4$) acts as a reducing agent, facilitating the conversion of 4-nitrophenol (4-NP) into 4-aminophenol (4-AP), a less toxic and more biodegradable compound. The ZnO NPs play a dual role in this process by adsorbing the reactant molecules and generating reactive species under sunlight. ZnO is well-known for its ability

to generate electron–hole pairs upon UV irradiation, which are critical for initiating and sustaining photocatalytic reactions. These electron–hole pairs drive the reduction of 4-NP into 4-AP through electron transfer reactions. The tailored bandgap of ZnO NPs synthesized *via* green methods enables efficient light absorption in the UV region, thus enhancing their photocatalytic efficiency under natural sunlight. Furthermore, their structural configuration promotes effective charge separation and minimizes electron–hole recombination, critical for achieving high photocatalytic performance. In summary, the unique properties of biogenic ZnO NPs make them a promising material for the photocatalytic degradation of persistent pollutants like 4-nitrophenol, offering an innovative and sustainable solution for environmental remediation.

5. Conclusion

This study presents a groundbreaking approach to the green synthesis of ZnO NPs mediated by *J. adhatoda*, achieving precise control over particle size, with an average size of 12.41 nm. This size tuning, combined with superior crystallinity and surface properties, positions these ZnO NPs as a benchmark for advanced NPs synthesis. The exceptional photocatalytic efficiency—demonstrated by 99.8% degradation of malachite green dye and rapid reduction of 4-nitrophenol—results from synergistic mechanisms involving ROS generation, direct electron–hole interactions, and enhanced dye adsorption. The integration of phytochemical capping agents minimizes electron–hole recombination, stabilizes charge carrier dynamics, and ensures robust NPs stabilization. By achieving unmatched particle size control, this study sets a new standard in NPs fabrication for environmental applications. These biogenic ZnO NPs offer a sustainable and scalable solution for pollution remediation while unlocking potential in advanced optoelectronic and catalytic systems. Future exploration of their application in industrial effluents and other environmental challenges will further enhance their impact.

Data availability

The data are available upon request.

Conflicts of interest

There are no conflicts to declare.

References

1 B. J. Singh, A. Chakraborty and R. Sehgal, A systematic review of industrial wastewater management: evaluating challenges and enablers, *J. Environ. Manage.*, 2023, **348**, 119230.
2 W. Artifon, *et al.*, Dyestuffs from textile industry wastewaters: trends and gaps in the use of bioflocculants, *Process Biochem.*, 2021, **111**, 181–190.
3 N. Puvaneswari, M. Jayarama and P. Gunasekaran, Toxicity assessment and microbial degradation of azo dyes, *Indian J. Exp. Biol.*, 2006, **44**, 618–626.
4 A. Kaur, *et al.*, Enhanced photocatalytic degradation and antimicrobial activities of biogenic Co_3O_4 nanoparticles mediated by fenugreek: sustainable strategies, *Mater. Adv.*, 2024, **5**(20), 8111–8131.
5 D. Jalandhara, *et al.*, A multifunctional Co-doped $BiFeO_3$ nanocomposite: a promising candidate for photocatalytic degradation, antibacterial activity, and antioxidant applications, *Mater. Adv.*, 2025, **6**, 641–657.
6 A. Khan, *et al.*, A comprehensive review on adsorptive removal of azo dyes using functional materials, *AQUA – Water Infrastructure, Ecosystems and Society*, 2024, **73**(2), 266–285.
7 P. Shandilya, P. Raizada, and P. Singh, Photocatalytic Degradation of Azo Dyes in Water, in *Water Pollution and Remediation: Photocatalysis*, ed. Inamuddin, M. I. Ahamed, and E. Lichtfouse, Springer International Publishing, Cham, 2021, pp. 119–146.
8 S. Rohilla, *et al.*, Excellent UV-Light Triggered Photocatalytic Performance of $ZnO.SiO_2$ Nanocomposite for Water Pollutant Compound Methyl Orange Dye, *Nanomaterials*, 2021, **11**(10), 2548.
9 W. Xie, *et al.*, Multidimensional TiO_2 photocatalysts for the degradation of organic dyes in wastewater treatment, *J. Porous Mater.*, 2024, **31**(5), 1655–1681.
10 Y. Deng and R. Zhao, Advanced Oxidation Processes (AOPs) in Wastewater Treatment, *Curr. Pollut. Rep.*, 2015, **1**(3), 167–176.
11 S. Aoudj, K. Bahloul, and A. Khelifa, Degradation of Dyes by Electrochemical Advanced Oxidation Processes, in *Advanced Removal Techniques for Dye-containing Wastewaters*, ed. S. S. Muthu and A. Khadir, Springer Singapore, Singapore, 2021, pp. 129–174.
12 A. Suguna, *et al.*, A detailed investigation on the structural, optical, and photocatalytic properties of ZnO@ZnS core–shell nanostructures, *J. Mater. Sci.: Mater. Electron.*, 2023, **34**(23), 1655.
13 Annin K. Shimi, *et al.*, Green synthesis of SrO nanoparticles using leaf extract of Albizia julibrissin and its recyclable photocatalytic activity: an eco-friendly approach for treatment of industrial wastewater, *Environmental Science: Advances*, 2022, **1**(5), 849–861.
14 J. Gaur, *et al.*, Current trends: zinc oxide NPs preparation *via* chemical and green method for the photocatalytic degradation of various organic dyes, *Hybrid Advances*, 2024, **5**, 100128.
15 P. Thi Lan Huong, *et al.*, Efficiency enhancement of photocatalytic activity under UV and visible light irradiation using ZnO/Fe_3O_4 heteronanostructures, *Sol. Energy*, 2023, **249**, 712–724.
16 D. A. de Souza, *et al.*, Easy and Fast Obtention of ZnO by Thermal Decomposition of Zinc Acetate and Its Photocatalytic Properties over Rhodamine B Dye, *Colorants*, 2024, **3**, 229–252, DOI: **10.3390/colorants3030016**.
17 Q. Zhang, *et al.*, Controlling oxygen vacancies and enhanced visible light photocatalysis of CeO_2/ZnO nanocomposites, *J. Photochem. Photobiol., A*, 2019, **392**, 112156.

18 K. C. Paradva, R. Jangir and S. Kalla, Green nanomaterials: synthesis and applications in wastewater treatment, *Inorg. Chem. Commun.*, 2023, **158**, 111584.
19 M. Y. Al-darwesh, S. S. Ibrahim and M. A. Mohammed, A review on plant extract mediated green synthesis of zinc oxide nanoparticles and their biomedical applications, *Results Chem.*, 2024, **7**, 101368.
20 A. Nyabadza, *et al.*, A review of physical, chemical and biological synthesis methods of bimetallic nanoparticles and applications in sensing, water treatment, biomedicine, catalysis and hydrogen storage, *Adv. Colloid Interface Sci.*, 2023, **321**, 103010.
21 N. S. Alsaiari, *et al.*, Plant and Microbial Approaches as Green Methods for the Synthesis of Nanomaterials: Synthesis, Applications, and Future Perspectives, *Molecules*, 2023, **28**(1), 463.
22 Y. Sridhar, *et al.*, Biosynthesis and characterization of gold nanoparticle from *Justicia adhatoda* and its catalytic activity, *Mater. Today: Proc.*, 2018, **5**, 8968–8972.
23 M. Nasir, *et al.*, Phytochemical Characterization and Assessment of Crude Extracts from *Justicia adhatoda* for Phytotoxic and Cytotoxic Activity, *Scientifica*, 2024, **2024**, 1374346.
24 M. Rudrapal, *et al.*, Valorization of *Adhatoda vasica* leaves: extraction, *in vitro* analyses and *in silico* approaches, *Front. Nutr.*, 2023, **10**, 1161471.
25 M. Gul, M. Kashif and K. Shahid, Eco-Friendly Approaches in the Synthesis of ZnO Nanoparticles using Plant Extract: A Review, *Phytopharmacology Research Journal*, 2024, **3**, 1–25.
26 R. Hamed, R. Obeid and R. Abu-Huwaij, Plant mediated-green synthesis of zinc oxide nanoparticles: an insight into biomedical applications, *Nanotechnol. Rev.*, 2023, **12**, 20230112.
27 X.-Q. Zhou, *et al.*, Zinc Oxide Nanoparticles: Synthesis, Characterization, Modification, and Applications in Food and Agriculture, *Processes*, 2023, **11**(4), 1193.
28 C. d. M. Strieder, *et al.*, Plant-mediated green synthesis of cerium oxide nanoparticles: a critical perspective of some unclear issues, *J. Mater. Res. Technol.*, 2024, **30**, 6376–6388.
29 M. Ramzan, *et al.*, Synergistic Effect of Zinc Oxide Nanoparticles and *Moringa oleifera* Leaf Extract Alleviates Cadmium Toxicity in *Linum usitatissimum*: Antioxidants and Physiochemical Studies, *Front. Plant Sci.*, 2022, **13**, 900347.
30 M. Mahajan, *et al.*, Surface-modified ZnO nanoparticles for enhanced environmental and biomedical performance, *Hybrid Advances*, 2025, **8**, 100342.
31 M. H. Kahsay, *et al.*, Green synthesis of zinc oxide nanostructures and investigation of their photocatalytic and bactericidal applications, *RSC Adv.*, 2019, **9**(63), 36967–36981.
32 N. Bala, *et al.*, Green synthesis of zinc oxide nanoparticles using *Hibiscus subdariffa* leaf extract: effect of temperature on synthesis, anti-bacterial activity and anti-diabetic activity, *RSC Adv.*, 2015, **5**(7), 4993–5003.
33 A. Fouda, *et al.*, Green Synthesis of Zinc Oxide Nanoparticles Using an Aqueous Extract of *Punica granatum* for Antimicrobial and Catalytic Activity, *J. Funct. Biomater.*, 2023, **14**(4), 205.
34 S. T. Karam and A. Fattah, Abdulrahman Green Synthesis and Characterization of ZnO Nanoparticles by Using Thyme Plant Leaf Extract, *Photonics*, 2022, **9**(8), 594.
35 X. Yang, *et al.*, Green Synthesis of Zinc Oxide Nanoparticles Using Aqueous Extracts of *Hibiscus cannabinus* L.: Wastewater Purification and Antibacterial Activity, *Separations*, 2023, **10**(9), 466, DOI: **10.3390/separations10090466**.
36 M. H. Kalaba, *et al.*, Green synthesis of zinc oxide nanoparticles (ZnO-NPs) by *Streptomyces baarnensis* and its active metabolite (Ka): a promising combination against multidrug-resistant ESKAPE pathogens and cytotoxicity, *BMC Microbiol.*, 2024, **24**(1), 254.
37 S. Faisal, *et al.*, Green Synthesis of Zinc Oxide (ZnO) Nanoparticles Using Aqueous Fruit Extracts of *Myristica fragrans*: Their Characterizations and Biological and Environmental Applications, *ACS Omega*, 2021, **6**(14), 9709–9722.
38 A. Raza, *et al.*, *Polyalthia longifolia*-mediated green synthesis of zinc oxide nanoparticles: characterization, photocatalytic and antifungal activities, *RSC Adv.*, 2024, **14**(25), 17535–17546.
39 J. Gaur, *et al.*, CTAB-crafted ZnO nanostructures for environmental remediation and pathogen control, *Sci. Rep.*, 2024, **14**(1), 20561.
40 J. Gaur, *et al.*, Photocatalytic degradation of Congo red dye using zinc oxide nanoparticles prepared using *Carica papaya* leaf extract, *Mater. Today Sustain.*, 2023, **22**, 100339.
41 M. K. Debanath and S. Karmakar, Study of blueshift of optical band gap in zinc oxide (ZnO) nanoparticles prepared by low-temperature wet chemical method, *Mater. Lett.*, 2013, **111**, 116–119.
42 N. Pandiyan, *et al.*, Ionic liquid – a greener templating agent with *Justicia adhatoda* plant extract assisted green synthesis of morphologically improved Ag–Au/ZnO nanostructure and it's antibacterial and anticancer activities, *J. Photochem. Photobiol. B Biol.*, 2019, **198**, 111559.
43 N. Matinise, *et al.*, ZnO nanoparticles *via Moringa oleifera* green synthesis: physical properties & mechanism of formation, *Appl. Surf. Sci.*, 2017, **406**, 339–347.
44 Z. M. Almarhoon, T. Indumathi and E. R. Kumar, Optimized green synthesis of ZnO nanoparticles: evaluation of structural, morphological, vibrational and optical properties, *J. Mater. Sci.: Mater. Electron.*, 2022, **33**(30), 23659–23672.
45 A. K. Tiwari, *et al.*, Spectroscopic investigations of green synthesized zinc oxide nanoparticles (ZnO NPs): antioxidant and antibacterial activity, *Discover Appl. Sci.*, 2024, **6**(8), 399.
46 K. Madi, *et al.*, Green Fabrication of ZnO Nanoparticles and ZnO/rGO Nanocomposites from Algerian Date Syrup Extract: Synthesis, Characterization, and Augmented Photocatalytic Efficiency in Methylene Blue Degradation, *Catalysts*, 2024, **14**(1), 62.

47 A. A. Barzinjy and H. H. Azeez, Green synthesis and characterization of zinc oxide nanoparticles using *Eucalyptus globulus* Labill. leaf extract and zinc nitrate hexahydrate salt, *SN Appl. Sci.*, 2020, **2**(5), 991.
48 M. M. Khan, *et al.*, Phytogenic Synthesis of Band Gap-Narrowed ZnO Nanoparticles Using the Bulb Extract of *Costus woodsonii*, *J. Bionanosci.*, 2019, **9**(2), 334–344.
49 S. W. Balogun, *et al.*, Green synthesis and characterization of zinc oxide nanoparticles using bashful (*Mimosa pudica*), leaf extract: a precursor for organic electronics applications, *SN Appl. Sci.*, 2020, **2**(3), 504.
50 A. Villegas-Fuentes, *et al.*, Improvement of the optical, photocatalytic and antibacterial properties of ZnO semiconductor nanoparticles using different pepper aqueous extracts, *Chemosphere*, 2023, **339**, 139577.
51 Y. V. Karpievitch, *et al.*, Liquid Chromatography Mass Spectrometry-Based Proteomics: Biological and Technological Aspects, *Ann. Appl. Stat.*, 2010, **4**(4), 1797–1823.
52 Y. A. Chesalov, G. B. Chernobay and E. V. Boldyreva, Temperature effects on the IR spectra of crystalline amino acids, dipeptides, and polyamino acids. II. L-and DL-serines, *J. Struct. Chem.*, 2008, **49**(4), 627–638.
53 Y. A. Selim, *et al.*, Green Synthesis of Zinc Oxide Nanoparticles Using Aqueous Extract of *Deverra tortuosa* and their Cytotoxic Activities, *Sci. Rep.*, 2020, **10**(1), 3445.
54 R. S. Sodhi, *et al.*, Biogenic synthesis of ZnO nanoparticles using *Polystichum squarrosum* extract and its applications as anti-oxidant, anti-diabetic agent and industrial waste water treatment, *Emergent Mater.*, 2024, **7**(1), 285–298.
55 M. Jeevarathinam and I. V. Asharani, Synthesis of CuO, ZnO nanoparticles, and CuO–ZnO nanocomposite for enhanced photocatalytic degradation of rhodamine B: a comparative study, *Sci. Rep.*, 2024, **14**(1), 9718.
56 D. K. Shrestha, *et al.*, Synthesis of Silver and Zinc Oxide Nanoparticles Using *Polystichum lentum* Extract for the Potential Antibacterial, Antioxidant, and Anticancer Activities, *J. Chem.*, 2024, **2024**(1), 1876560.
57 R. K. Chaudhari, P. A. Shah and P. S. Shrivastav, Green synthesis of silver nanoparticles using *Adhatoda vasica* leaf extract and its application in photocatalytic degradation of dyes, *Discover Nano*, 2023, **18**(1), 135.
58 C. A. Fernandes, *et al.*, Biogenic Synthesis of Zinc Oxide Nanoparticles Mediated by the Extract of *Terminalia catappa* Fruit Pericarp and Its Multifaceted Applications, *ACS Omega*, 2023, **8**(42), 39315–39328.
59 R. E. Watson and L. H. Bennett, A Mulliken electronegativity scale and the structural stability of simple compounds, *J. Phys. Chem. Solids*, 1978, **39**(11), 1235–1242.
60 C. Wang, H. Wang and Y. Cao, Ultrasonic improvement of catalytic decomposition of rhodamine B in simulated wastewater by functional waste printed circuit boards *via* thermochemical conversion, *J. Cleaner Prod.*, 2020, **253**, 119921.
61 Z. Yu, *et al.*, Micronleaf-shape graphene interfaces on wood transverse sections as advanced photothermal evaporators for water purification, *J. Mater. Sci. Technol.*, 2024, **193**, 81–89.
62 N. Yudasari, M. M. Suliyanti and C. Imawan, Antibacterial activity of Fe-doped ZnO nanoparticles synthesised *via* pulsed laser ablation in liquid against *Staphylococcus aureus*, *Adv. Nat. Sci.:Nanosci. Nanotechnol.*, 2020, **11**(2), 025003.
63 A. Taufiq, *et al.*, Effects of ZnO nanoparticles on the antifungal performance of Fe_3O_4/ZnO nanocomposites prepared from natural sand, *Adv. Nat. Sci.:Nanosci. Nanotechnol.*, 2020, **11**(4), 045004.
64 E. Abdelkader, N. Laouedj and A. Bekka, ZnO-Assisted Photocatalytic Degradation of Congo Red and Benzopurpurine 4B in Aqueous Solution, *J. Chem. Eng. Process Technol.*, 2011, **2**, 1–9.
65 K. K. Supin, P. M. Parvathy Namboothiri and M. Vasundhara, Enhanced photocatalytic activity in ZnO nanoparticles developed using novel *Lepidagathis ananthapuramensis* leaf extract, *RSC Adv.*, 2023, **13**(3), 1497–1515.
66 S. Sasi, *et al.*, Green synthesis of ZnO nanoparticles with enhanced photocatalytic and antibacterial activity, *J. Alloys Compd.*, 2022, **924**, 166431.
67 M. A. Fagier, Plant-Mediated Biosynthesis and Photocatalysis Activities of Zinc Oxide Nanoparticles: A Prospect towards Dyes Mineralization, *J. Nanotechnol.*, 2021, **2021**(1), 6629180.
68 S. B. Ruvubu and I. Roy, Eco-friendly synthesis and surface modification of ZnO nanoparticles using *Pueraria montana* root extract: enhanced photocatalytic performance with trisodium pyrophosphate, *Int. J. Environ. Anal. Chem.*, 2024, **7**, 1–43.
69 E. Abroushan, S. Farhadi and A. Zabardasti, Ag_3PO_4/$CoFe_2O_4$ magnetic nanocomposite: synthesis, characterization and applications in catalytic reduction of nitrophenols and sunlight-assisted photocatalytic degradation of organic dye pollutants, *RSC Adv.*, 2017, **7**(30), 18293–18304.
70 K. Bano, *et al.*, Sunlight driven photocatalytic degradation of organic pollutants using a MnV_2O_6/$BiVO_4$ heterojunction: mechanistic perception and degradation pathways, *Nanoscale Adv.*, 2021, **3**(22), 6446–6458.
71 J. Kubelka and T. A. Keiderling, *Ab Initio* Calculation of Amide Carbonyl Stretch Vibrational Frequencies in Solution with Modified Basis Sets. 1. *N*-Methyl Acetamide, *J. Phys. Chem.*, 2001, **105**(48), 10922–10928.
72 Y. Liu, *et al.*, Synthesis of lignin-derived nitrogen-doped carbon as a novel catalyst for 4-NP reduction evaluation, *Sci. Rep.*, 2020, **10**(1), 20075.